Monthly Notices of the ROYAL ASTRONOMICAL SOCIETY

MNRAS **541,** 2955–2977 (2025) https://doi.org/10.1093/mnras/staf1108
Advance Access publication 2025 July 07

Search for periodic variability in γ-ray blazars Using *Fermi*-LAT

P. Peñil [1]★ M. Ajello [1]★ S. Buson [2,3]★ A. Domínguez [4] J.R. Westernacher-Schneider [5] A. Rico [1] S. Adhikari [1] and J. Zrake [1]

[1]*Department of Physics and Astronomy, Clemson University, Kinard Lab of Physics, Clemson, SC 29634-0978, USA*
[2]*Julius-Maximilians-Universität Würzburg, Fakultät für Physik und Astronomie, Emil-Fischer-Str 31, D-97074 Würzburg, Germany*
[3]*Deutsches Elektronen-Synchrotron DESY, Platanenallee 6, D-15738 Zeuthen, Germany*
[4]*IPARCOS and Department of EMFTEL, Universidad Complutense de Madrid, E-28040 Madrid, Spain*
[5]*Westgate Research, PO Box 181, Cardiff, ON K0L 1M0, Canada*

Accepted 2025 July 4. Received 2025 July 1; in original form 2025 April 4

ABSTRACT

Blazars are known to exhibit variability across a broad range of time-scales. This behaviour can include periodicity in their γ-ray emission, whose clear detection remains an ongoing challenge, partly due to the inherent stochasticity of the processes involved and also the lack of adequately well-sampled light curves. In this study, we perform a systematic search for periodicity in a selected sample of 24 γ-ray blazars using twelve years of *Fermi*-LAT data. The sample comprises the most promising candidates selected from a previous study, extending the light curves by three additional years, expanding the analysed energy range from >1 to >0.1 GeV to improve photon statistics, and enhancing the time-series analysis methodology. We incorporate upper-limit flux points in the analysis rather than discarding them, thereby preserving the temporal structure in the light curves. A suite of seven complementary time-series analysis methods is employed to ensure statistical robustness, including autoregressive models, representing a methodological advancement over the prior work. A further improvement is the explicit estimation of the look-elsewhere effect, which allows us to assess the global significance of any detected signals. The study is also supported by additional statistical treatments employed to minimize false detections and strengthen the reliability of the results. Our analysis reveals a hint of periodicity in PG 1553+113 with a global significance of $\approx 1.8\sigma$. For the remaining sources in the sample, the re-evaluation of previously reported periodicities indicates that they are statistically consistent with arising from stochastic variability.

Key words: galaxies: active – BL Lacertae objects: general.

1 INTRODUCTION

Active galactic nuclei (AGNs), i.e. galaxies with an accreting supermassive black hole (SMBH) in the centre, are among the most luminous persistent objects in the Universe (e.g. Soltan 1982; Cavaliere & Padovani 1989; Wiita 2006). The complex interplay between the black hole hosted at the AGN core and the surrounding circumnuclear gas leads to the formation of an accretion disc and may influence the properties of the host galaxy (e.g. the stellar mass of the inner bulge, Häring & Rix 2004). A small fraction of AGN is distinguished by the presence of a pair of highly collimated, relativistic jets. These jets typically form in opposite directions, perpendicular to the rotational plane of the SMBH-accretion disc system. When one of the jets is closely aligned with the line of sight, the object is referred to as a blazar. The observed emission from blazars is strongly dominated by the jet, spans energies ranging from radio to γ-rays, and can be highly variable on time scales ranging from seconds to years (e.g. Urry 1996, 2011).

During their cosmological evolution galaxies can merge (e.g. Jiang, Hogg & Blanton 2012), frequently at moderate/high redshifts (e.g. Rieger 2007; Lin et al. 2008) when they are also more gas-rich (e.g. Tacconi et al. 2010). In the process of an AGN merger, one expects that the two SMBHs hosted at the respective centres eventually meet and form a binary system with a typical separation of about kiloparsec (Begelman, Blandford & Rees 1980). Such a binary system is referred to as a supermassive black hole binary (SMBHB). As a consequence of dynamical friction, the SMBHs can converge to the centre of mass of the galaxy and shrink their separation down to sub-parsec distances (e.g. Dosopoulou & Antonini 2017). Finally, the last stage of merging is the coalescence of the SMBHBs into a single SMBH (e.g. Colpi 2014), resulting in one of the loudest sources of gravitational waves in the Universe (e.g. Enoki et al. 2004).

The identification of SMBHB systems with sub-parsec separation is an important topic of astrophysics, but remains challenging since they cannot generally be spatially resolved and are rare. Limits on the nanohertz stochastic gravitational wave background from the Pulsar Timing Array (PTA, Holgado et al. 2018; Rieger 2019) suggest that only a minor fraction ($\lesssim 0.01$–0.1 per cent) of blazars could be harboring SMBHBs with sub-parsec separations (e.g. Liu

★ E-mail: ppenil@clemson.edu (PP); majello@clemson.edu (MA); sara.buson@uni-wuerzburg.de (SB)

et al. 2014). Such SMBHBs could imprint peculiar time-variability patterns in their emitted radiation with periods of one year.

One of the strategies employed to pinpoint candidate SMBHBs has been the search for periodic modulation, also known as quasi-periodic oscillations, in AGN light curves (LCs). The detection of periodicity in blazars has been limited by the lack of continuous and sensitive long-term sampling. Recently, the Large Area Telescope (LAT) on board the *Fermi Gamma-ray Space Telescope* has alleviated this issue by scanning the entire sky regularly with high sensitivity (Atwood et al. 2009). During more than a decade of continuous monitoring, since *Fermi* was launched in 2008, the LAT has collected a wealth of valuable data, offering the unprecedented opportunity to monitor flux variations from thousands of blazars in the GeV band. Densely sampled, unbiased, high-quality LCs are now accessible for all sources in the LAT catalogues. The fourth *Fermi*-LAT source catalog (4FGL; Abdollahi et al. 2020; Ballet et al. 2020) is based on the first 8 years of LAT observations and includes more than 5000 sources, among which about 3000 are confidently associated with blazar counterparts. Recently, the 4FGL-DR3 catalogue (Data Release 3) has been published, which is based on the first 12 yr of LAT observations (Abdollahi et al. 2022).

Searching for periodicity in a time series (an ordered sequence of fluxes as a function of time) requires measuring the power of the time series at each frequency and identifying the dominant frequency, if any. This information is captured in periodograms, which are obtained through a variety of techniques such as Lomb–Scargle (Lomb 1976; Scargle 1982) and wavelets (Foster 1996; Torrence & Compo 1998). For the most part, studies in the literature that search for periodicity in blazar γ-ray LCs have mainly focused on a few selected objects and typically have employed at most two or three time-series algorithms (e.g. Zhang et al. 2017a; Tavani et al. 2018; Bhatta & Dhital 2020). These previous studies found a few candidates with periodicity (e.g. PG 1553+113 or OJ 287; Ackermann et al. 2015; Valtonen et al. 2016, respectively) but due to the stochastic nature of emission in blazars, these findings remain under debate (e.g. Covino, Sandrinelli & Treves 2018). As a pioneering investigation in Peñil et al. (2020,, P20, hereafter), we performed a comprehensive search for periodicities in blazar γ-ray LCs, targeting $\sim$2000 blazars and adopting ten of the most used methods for time-series analysis. Our effort discovered 24 periodic blazar candidates with local (pre-trial) significance above 2.5σ.

In the work presented here, we reanalyse the 24 candidates from P20, employing new data that cover three additional years of *Fermi*-LAT observations. We apply a similar periodicity-detection pipeline as the one described by P20 and include new statistical methods. Specifically, we also use the autoregressive models Autoregressive Integrated Moving Average (ARIMA) and Autoregressive Fractionally Integrated Moving Average (ARFIMA) to deal with the stochastic uncertainty introduced by noise in the periodicity search. Finally, we also take into account the look-elsewhere effect to provide robust significance for the detected periods.

The paper is organized as follows. In Section 2, the blazar sample and data reduction methodology are presented. Then, Section 3 details the periodicity analysis methodology, and Section 5 shows and discusses our results. In Section 6, there is a description of the potential interpretation of the results focusing on the two sources with the most significant periodicity. We summarize the findings in Section 7.

2 GAMMA-RAY SAMPLE

2.1 *Fermi*-LAT data reduction

The *Fermi*-LAT data are reduced with the PYTHON package FERMIPY (Wood et al. 2017). The following procedure is adopted for each source in the sample. We select photons of the `Pass 8 SOURCE` class (Atwood et al. 2013; Bruel et al. 2018), in a region of interest (ROI) of $15^\circ \times 15^\circ$ square, centred at the target. To minimize the contamination from γ rays produced in the Earth's upper atmosphere, a zenith angle cut of $\theta < 90^\circ$ is applied. We also applied the standard data quality cuts (DATA_QUAL > 0)&&(LAT_CONFIG $== 1$) and removed time periods coinciding with solar flares and γ-ray bursts detected by the LAT. The ROI model includes all 4FGL-DR2 catalog sources (Ballet et al. 2020) located within 20° from the ROI centre, as well as the Galactic and isotropic diffuse emission[1] (`gll_iem_v07.fits` and `iso_P8R3_SOURCE_V2.txt`).

We perform a binned analysis in the 0.1–800 GeV energy range, using 10 bins per decade in energy and 0.1° spatial bins, and adopting the `P8R3_SOURCE_V2` instrument response functions. First, a maximum likelihood analysis is performed over the full-time range considered here, i.e. 2008 Aug 04 15:43:36 UTC to 2020 Dec 10 00:01:26 UTC. In the fit, we model the sources in the ROI, adopting the spectral shapes and parameters reported in 4FGL. We allow the normalization and spectral index of the target source to vary, as well as the normalizations of all sources within 3° of the ROI centre and the isotropic and Galactic diffuse components. Since our data span a different integration time with respect to 4FGL, our first results are checked for potential newly detected sources with an iterative procedure. To this aim, a test statistic (TS) map is produced. The TS is defined as $2\log(L/L_0)$, where L is the likelihood of the model with a point source at a given position and L_0 is the likelihood without the source. A TS value of 25 corresponds to a statistical significance of $\gtrsim 4.0\sigma$ (according to the prescription adopted in Mattox et al. 1996; Abdollahi et al. 2020). A TS map is produced by including a putative point source at each pixel of the map and evaluating its significance over the current best-fitting model. The test source is modelled with a power-law spectrum where only the normalization is allowed to vary in the fit, whereas the photon index is fixed at 2. We look for significant peaks (TS > 25) in the TS map, with a minimum separation of 0.5° from existing sources in the model, and add a new point source to the model at the position of the most significant peak found. Then, the ROI is fitted again, and a new TS map is produced. This process is iterated until no more significant excesses are found, generally leading to the addition of two point sources.

To produce the LCs, we split the data for each source into 28-d bins and perform a full likelihood fit in each time bin. For the likelihood fits of the time bins, the best-fitting ROI model obtained from the full-time interval analysis is adopted. We first attempt a fit allowing variation in the normalizations of the target and of all sources in the inner 3° of the ROI, along with the diffuse components. If the fit does not converge, the number of free parameters is progressively restricted in the fit in an iterative way until the fit successfully converges. We begin this iterative process by fixing sources in the ROI that are weakly detected (i.e. with TS$<$4). Next, we fix sources with TS$<$9. Then, we fix sources up to 1° from the ROI centre and

[1] https://fermi.gsfc.nasa.gov/ssc/data/access/lat/BackgroundModels.html

Table 1. Comparison of periods and local test statistics for the blazars analysed in P20. The test statistics and periods reported here are the averages of those obtained in the different methods employed in the periodicity-search analysis (to allow a comparison with P20). From *top* to the *bottom*: $> 3\sigma$ candidates and low-significance candidates. The candidates are sorted according to the median of their test statistics. Note that this median significance does not have an actual statistical meaning; it is used as an arbitrary way to combine all test statistics to sort the candidates. The blazars are characterized by their *Fermi*-LAT 4FGL source name, equatorial coordinates (deg), AGN type, redshift, association name, period (in years), and test statistics obtained by Peñil et al. (2020), and the average period (in years) and test statistics obtained in this work. We include the percentage of upper limits (UL) in the LC. We also included the global significance in the last column resulting from the method described in Section 4.1. Note that some sources have two significant periods (organized by the peak amplitude), denoted by ⋆.

4FGL Source name	RA(J2000)	Dec(J2000)	Type	Redshift	Association name	UL (%)	P20 Period [yr] (S/N)	Period [yr] (S/N)	Global (S/N)
J1555.7+1111	238.93169	11.18768	bll	0.433	PG 1553+113	0 per cent	2.2 ($> 4.0\sigma$)	2.2 (4.5σ)	$1.8\,\sigma$
J2158.8−3013	329.71409	−30.22556	bll	0.116	PKS 2155−304	0 per cent	1.7 ($> 3.0\sigma$)	1.7 (3.3σ)	$\approx 0\sigma$
J0811.3+0146	122.86418	1.77344	bll	1.148	OJ 014	0.6 per cent	4.3 ($> 3.5\sigma$)	4.1 (2.9σ)	$\approx 0\sigma$
J0457.0−2324	74.26096	−23.41384	fsrq	1.003	PKS 0454−234	0 per cent	2.6 ($> 2.5\sigma$)	3.6 (2.8σ)	$\approx 0\sigma$
J0721.9+7120⋆	110.48882	71.34127	bll	0.127	S5 0716+714	0 per cent	2.8 ($> 2.5\sigma$) 0.9 ($> 2\sigma$)	2.7 (2.8σ) 0.9 (2.0σ)	$\approx 0\sigma$
J0043.8+3425	10.96782	34.42687	fsrq	0.966	GB6 J0043+3426	4.9 per cent	1.8 (4.0σ)	1.9 (2.7σ)	$\approx 0\sigma$
J0521.7+2113	80.44379	21.21369	bll	0.108	TXS 0518+211	0 per cent	2.8 ($> 3.0\sigma$)	3.1 (2.6σ)	$\approx 0\sigma$
J1649.4+5238	252.35208	52.58336	bll	–	87GB 164812.2+524023	12 per cent	2.7 ($> 2.5\sigma$)	2.8 (2.2σ)	$\approx 0\sigma$
J0449.4−4350	72.36042	−43.83719	bll	0.205	PKS 0447−439	0 per cent	2.5 (3.0σ)	1.9 (2.1σ)	$\approx 0\sigma$
J0428.6−3756	67.17261	−37.94081	bll	1.11	PKS 0426−380	0 per cent	3.4 (3.0σ)	3.6 (2.1σ)	$\approx 0\sigma$
J0303.4−2407	45.86259	−24.12074	bll	0.266	PKS 0301−243	0 per cent	2.0 (3.0σ)	2.1 (2.0σ)	$\approx 0\sigma$
J1146.8+3958	176.73987	39.96861	fsrq	1.089	S4 1144+40	0.6 per cent	3.3 ($> 3.0\sigma$)	3.3 (1.9σ)	$\approx 0\sigma$
J1248.2+5820	192.07728	58.34622	bll	–	PG 1246+586	0 per cent	2.0 (3.0σ)	2.1 (1.9σ)	$\approx 0\sigma$
J0252.8−2218	43.20377	−22.32386	fsrq	1.419	PKS 0250−225	1.2 per cent	1.2 ($> 2.5\sigma$)	1.2 (1.7σ)	$\approx 0\sigma$
J2258.0−2759⋆	344.50485	−27.97588	fsrq	0.926	PKS 2255−282	8.1 per cent	1.3 ($> 3.5\sigma$)	2.8 (1.7σ) 1.4 (1.1σ)	$\approx 0\sigma$
J1903.2+5541	285.80851	55.67557	bll	–	TXS 1902+556	0 per cent	3.8 ($> 2.5\sigma$)	3.3 (1.5σ)	$\approx 0\sigma$
J0501.2−0157	75.30886	−1.98359	fsrq	2.291	S3 0458−02	1.8 per cent	1.7 ($> 2.5\sigma$)	3.8 (1.4σ)	$\approx 0\sigma$
J1303.0+2435	195.75454	24.56873	bll	0.993	MG2 J130304+2434	9.9 per cent	2.0 ($> 2.5\sigma$)	2.1 (1.2σ)	$\approx 0\sigma$
J2056.2−4714⋆	314.06768	−47.23386	fsrq	1.489	PKS 2052−47	0 per cent	1.7 ($> 2.5\sigma$)	3.1 (1.1σ) 1.7 (2.2σ)	$\approx 0\sigma$
J0818.2+4223	124.56174	42.38367	bll	0.530	S4 0814+42	0 per cent	2.2 (3.5σ)	2.2 (0.8σ)	$\approx 0\sigma$
J0211.2+1051	32.81532	10.85811	bll	0.2	MG1 J021114+1051	0.6 per cent	1.7 ($> 3.5\sigma$)	2.9 (0.8σ)	$\approx 0\sigma$
J0102.8+5825	15.71134	58.41576	fsrq	0.644	TXS 0059+581	4.3 per cent	2.1 (3.0σ)	4.0 (0.8σ)	$\approx 0\sigma$
J1454.5+5124	223.63225	51.413868	bll	–	TXS 1452+516	0.6 per cent	2.1 ($> 3.5\sigma$)	2.1 (0.7σ)	$\approx 0\sigma$
J0210.7−5101	32.68952	−51.01695	fsrq	1.003	PKS 0208−512	0 per cent	2.6 ($> 3.0\sigma$)	3.8 (0.1σ)	$\approx 0\sigma$

those with TS<25. Finally, we fix all parameters except the target source's normalization. We consider the target source to be detected when TS>1 in the corresponding time bin. Whenever this condition is not fulfilled, a 95 per cent confidence upper limit is reported from the likelihood distribution (Peñil et al. 2025). These points are denoted by down arrows in the plots of the LCs (Fig. A1).

2.2 Source selection

The blazar sample in P20 was analysed using 9 yr of *Fermi*-LAT observations (see Table 1). In this work, we reanalyse the 24 periodicity candidates similarly pinpointed in P20 but with several improvements:

(i) Extend the observing time to 12 yr, from 2008 August until 2020 December.

(ii) Expand the energy range from > 1 to > 0.1 GeV, thus increasing the photon statistics, improving the signal-to-noise ratio, and dramatically reducing the number of upper limits in the LCs. For example, S4 1144+40 had a fraction of 40 per cent upper limits in P20, which is reduced to <1 per cent here.

(iii) Retain the information for the LC points with low statistics (i.e. non-detection) by substituting the upper-limit data with the flux value that maximizes the likelihood function for that time bin (Peñil et al. 2025). The likelihood function is scanned in the same way for bins that result in a positive detection and for bins where typically an upper limit is reported (instead of the best fit flux with uncertainties). Here, we use the best-fitting flux (and its uncertainty) regardless of the statistical significance (TS) in that bin.

To evaluate whether the substitution of upper-limit data points introduces any bias into the periodicity analysis, we conduct a test using the two sources in our sample with the highest percentage of gaps in their LCs (see Table 1): 87GB164812.2+524023 (12 per cent) and MG2J130304+2434 (9.9 per cent). In this test, we remove all upper-limit points from the LCs. We then apply two of the methods from our analysis framework, the Lomb–Scargle Periodogram and Phase Dispersion Minimization, both of which are suitable for analysing irregularly sampled time series.

The results obtained from the gappy LCs are consistent with those derived from the original versions, where upper limits are retained through substitution. Specifically, we obtain the same periodicities and similar values for the associated test statistics in both cases. These findings align with those reported in P20, where it was shown that the influence of observational gaps becomes statistically significant when the gap fraction reaches or exceeds ∼50 per cent. Therefore, for moderate levels of missing data, our substitution strategy appears

to be a robust approach that preserves the integrity of the periodicity search.

Finally, we use the same 28-d binning for the LCs. This time binning provides an adequate compromise between a computationally manageable analysis and sensitivity to long-term variations (of the order of a year).

3 METHODOLOGY

3.1 Overview of methodology

Periodicity searches are limited in part by noise. Many Galactic and extragalactic astrophysical sources show erratic brightness fluctuations with steep power spectra (e.g. Gao, Cao & Lee 2003). In this context, the noise is defined as random variations in the source emission. Noise is classified according to the power-law index β of the power spectral density (PSD, $\propto f^{-\beta}$ where f is frequency, Rieger 2019). The PSD measures the power in a signal as a function of the frequency. White, pink, and red noises are characterized by indices of $\beta = 0$, $\beta = 1$, and $\beta = 2$, respectively (e.g. Tarnopolski et al. 2020).

The statistical significance of any putative periodicities must be evaluated in the context of this stochastic noise. We therefore identify two challenges: (1) to search for and identify periodicities in the large data set of LCs and (2) to determine the statistical significance of the periodicity given the characteristics of the noise appropriate for each source.

To search for the periodic signals, we have developed a pipeline that applies a number of standard periodicity-search algorithms to the data set. The details of the algorithms are given in Sections 3.2 and 3.3. Each algorithm searches for periods across a given frequency range and produces a test statistic from which potentially interesting periodic signals can be identified. The test statistic for each algorithm is computed by evaluating the amplitude of the periodicity against an alternative (null) hypothesis that can be rapidly evaluated. Tables A1 and A5 list the results of this pipeline with the period and test-statistic value for the most promising periodicity candidates. Details are given in the following sections.

We evaluate the statistical significance of any potentially interesting periodicities identified by the pipeline using a Monte Carlo procedure in which a large number of artificial LCs are generated using the method of Emmanoulopoulos, McHardy & Papadakis (2013) using a stochastic model whose parameters have been fitted to the observed LC, as described in Section 4.3. The statistical significance found from this procedure is presented in Table A1. In Section 4.1, we also evaluate the impact of the 'look-elsewhere' effect on our results.

Finally, we search for long-term (∼years) periodicity since we are looking for blazars to be SMBHB candidates in the gas-driven regime (see Section 6). Consequently, we search for periods in the [1–6] year range. While a study of shorter periods (e.g. ∼months) would suffer less contamination due to red noise, other challenges appear. First, the smaller bins contain fewer γ-ray photons, so the statistical uncertainty per bin is larger. Second, in the context of searching for binaries, the residence time at a given orbital period $t_{\rm orb}$ scales as $t_{\rm orb}^{8/3}$ in the gravitational wave-driven regime (Haiman, Kocsis & Menou 2009). Thus, considering month-long periods rather than year-long periods would reduce the expected number of binaries in the sample by more than 99 per cent. On the other hand, this also implies that any periodicity found shorter than ∼year-long is more likely to be due to other processes, e.g. disk and/or jet procession from a single SMBH. These alternative processes are interesting in their own right, and we intend to explore shorter periods in future works.

3.2 Periodicity search methods

Careful considerations must be taken in a periodicity-search analysis. In general, each method has specific properties, e.g. accuracy, computational time, and sensitivity to irregular time series. Therefore, selecting just one time-series method is arguably arbitrary since all have limitations and advantages (Goyal et al. 2017; VanderPlas 2018). Consequently, we want to profit from the strengths of the many different algorithms in the literature in detecting periodicities, compare their results systematically, and provide the community with a comprehensive search for periodicity in which reasonable algorithms have been used, helping other researchers in their analysis. In light of this, we employed in P20, 10 of the most widely used methods for periodicity identification to reduce the impact of their individual limitations and take advantage of their individual strengths. These ten methods were organized in a pipeline described in P20, to which we refer the reader for further details.

However, this pipeline has some caveats. In P20, we used the bootstrap and Fisher's method of randomization (Linnell Nemec & Nemec 1985) to infer the test statistics, which assume white noise as a null hypothesis. This assumption is not correct since the intrinsic variability in blazars is red-noise-like (Vaughan et al. 2016). To solve this, we substitute these techniques by generating artificial LCs based on a power-law approach using the technique presented by Timmer & Koenig (1995). The generated artificial LCs have the same standard deviation, median flux, and sampling as the original LCs. An LC produced with this technique is based on a Gaussian-like LC generation, but the γ-ray flux is log-normal distributed (e.g. Shah et al. 2018). Shah, Misra & Sinha (2020) obtains the log-normal distribution by exponentiating the LC. Furthermore, this technique is fast, which is a requirement for the first analysis stage of the pipeline. For the remaining methods, we use the strategy described by Emmanoulopoulos et al. (2013), which allows the generation of LCs with the same PSD and probability density function as real blazar LCs. Following Emmanoulopoulos et al. (2013), we generate LCs by applying the bending-power law approach (Chakraborty & Rieger 2020), defined by the expression:

$$P(\nu) = A\left(1 + \left\{\frac{\nu}{\nu_b}\right\}^{\alpha}\right)^{-1} + C, \tag{1}$$

where A is the normalization (rms^2/yr^{-1}), the spectral index is α, and the bending frequency is ν_b. This approach provides realistic models of blazars' variability on time-scales from weeks to years (Chakraborty & Rieger 2020).

Poisson noise is a form of statistical noise that arises due to the inherent randomness in the counting of photons, particularly prevalent in the high-energy range, such as gamma rays. This type of noise leads to fluctuations in the count rate of detected photons, resulting in variability in the observed LC of a blazar. Given that each photon arrival is a random event, the LC will naturally exhibit statistical variations, even if the source's actual flux remains constant. Poisson noise contributes a constant (white noise) to the power spectrum. The value of this constant is estimated using the following expression:

$$C = \frac{2D}{N\bar{x}^2}\bar{\Delta x^2}, \tag{2}$$

Where D is the total time duration of the LC, $\bar{x}$ is the mean flux, $\bar{\Delta x^2}$ represents the average squared error of the flux uncertainties,

and N the number of data in the LC. We incorporate Gaussian-distributed random errors, matching the characteristics observed in the actual data to the artificial LCs. This inclusion serves to represent the presence of Poisson noise.

In addition to that, we removed the REDFIT from the pipeline (Schulz & Mudelsee 2002). REDFIT assumes an AR(1) (first-order autoregressive process) to model the red noise process, which is inappropriate for blazars (Vaughan 2010). Additionally, the test statistics estimation assumes a single, best fit, which overestimates the test statistics (e.g. Vaughan 2010; Vaughan et al. 2016).

Therefore, in this work, we use the methods listed below[2]:

(i) Lomb–Scargle periodogram (LSP, Lomb 1976; Scargle 1982) which is superposed on a red noise spectrum to obtain the test statistics (Vaughan 2005).

(ii) Generalized Lomb–Scargle periodogram (GLSP; Zechmeister & Kürster 2009).

(iii) Phase dispersion Mminimization (PDM; Stellingwerf 1978).

(iv) Continuous Wavelet Transform (CWT; Torrence & Compo 1998).

(v) Markov Chain Monte Carlo Sinusoidal Fitting (MCMC Sine; Foreman-Mackey et al. 2013). This method allows us to obtain a model of the oscillating signal, characterizing the offset, amplitude, period, and phase. This information is used to evaluate the performance of the other methods against the noise (see Section 4.4).

The test statistics for the peaks in the periodicity analysis are determined by generating 1000 000 artificial LCs using the method described in Emmanoulopoulos et al. (2013) for both the GLSP and CWT methods. The test statistic is defined as the fraction of simulated LCs in which the power at any frequency within the studied range exceeds the highest peak observed in the original LC. This process limits the statistical significance to a maximum of $\approx 4.9\sigma$. For the PDM method, due to computational constraints, 150 000 artificial LCs are generated, limiting the statistical significance at $\approx 4.5\sigma$.

Additionally, the choice of the number of artificial LCs directly affects the precision of the test statistics estimation. While the large sample size for GLSP and CWT ensures more accurate significance levels, the computational demands of PDM limit its precision, though it still provides reliable estimates for most practical purposes.

Finally, we use new methods described in the following sections in this current work.

3.3 Autoregressive models

In this work, we include autoregressive models to improve our analysis pipeline. These models are proposed as efficient methods for astronomical data analysis, particularly to infer any periodic behaviour (Scargle 1981; Caceres et al. 2019). To analyze the *Fermi*-LAT LCs, the ARIMA (Chatfield 2004), and ARFIMA (Feigelson, Babu & Caceres 2018) are applied. These autoregressive models are suitable for analysing astronomical time series since they allow modeling a wide variety of LC properties (e.g. irregular or quasi-periodic, constant mean or variable mean) or combinations of stochastic and deterministic behaviours (Feigelson et al. 2018). These characteristics make these models more robust against stochastic noise, helping to infer periodic behaviours more accurately (Caceres et al. 2019).

Both models are based on an autocorrelation (correlation of the LC with itself) where one looks for dependencies of the current values (of the LC) on past values. In this approach, the current values are modelled as the sum of two linear combinations of past values (with p and q terms, respectively) that model an autoregressive and stochastic process, respectively (see Feigelson et al. 2018, for details). The parameter d in ARIMA represents how stationary the LC is, i.e. whether a time series has a constant mean and variance (in which case, $d = 0$). In ARFIMA, the parameter d represents the type of process. For instance, $0< d <1$ corresponds to a long memory process, while $-0.5 < d < 0$ is a short memory process. This parameter is in the 0–0.5 range for a stationary time series. A stochastic process is modeled as ARFIMA(1,d,0) (Xu 2019), and ARIMA(0,0,1) (Zhang et al. 2020).

In our methodology, the ARFIMA model can be applied to stationary time series. ARFIMA can model non-stationary series, but it is not recommended due to potential inconsistencies in its applications (Baillie 1996). ARIMA models are preferred for non-stationary time series because they are specifically designed to address this characteristic through integer differencing (see, Caceres et al. 2019). Stationarity is measured using the augmented Dickey–Fuller unit root test (Dickey & Fuller 1979), which tests the null hypothesis that a time series is non-stationary. For the purposes of this study, we reject the null hypothesis if the p-value is ≤ 0.05.

The periodicity search with these methods begins with selecting the best-fitting ARFIMA/ARIMA model using Akaike's Information Criterion (AIC, Akaike 1973). The AIC is a statistical estimator that evaluates a model that fits the data. AIC is used to compare models to determine which one performs the best fit for the data. After that, the residuals are obtained from the original LC and the selected ARFIMA/ARIMA model. Then, we compute the autocorrelation function (ACF) on these residuals (see Fig. 4). We use the same criterion presented in the literature by using a $\geqslant 2\sigma$ threshold for test statistics (e.g. Zhang et al. 2017c, 2020; Yang et al. 2021). Finally, we use the Ljung–Box test to evaluate the quality of fit between the LC and its ARFIMA/ARIMA model (Ljung & Box 1978). The Ljung–Box test checks whether or not the autocorrelations for the residuals are non-zero, denoting the lack (or not) of model fit. We consider the fit adequate when the p-value is at least 0.05. Higher p-values mean that the ARFIMA/ARIMA model fits the LC better.

To implement the ARFIMA/ARIMA analysis, we use the R packages `stats`[3] and `arfima`[4] This R functionality is accessible from a Python environment via the package `rpy2`.[5]

With ARIMA and ARFIMA.[6], the total number of methods used in the analysis is seven.

[2]The computational times required to perform atomic operations for each method are as follows: LSP ($1.1\text{x}10^{-3}$ *s*), GLSP ($6.5\text{x}10^{-4}$ *s*), PDM ($2.9\text{x}10^{-3}$ *s*), CWT ($2.2\text{x}10^{-3}$ *s*), and MCMC Sine ($7.1\text{x}10^{-1}$ *s*). These results are obtained using the LC of PG 1553+113. All computations were carried out on a system equipped with an Intel(R) Core(TM) i7-5500U CPU running at 2.40 GHz (dual-core, 4 logical processors) and 16 GB of RAM.

[3]https://www.rdocumentation.org/packages/stats/versions/3.6.2/topics/arima

[4]https://www.rdocumentation.org/packages/forecast/versions/8.13/topics/arfima

[5]https://rpy2.github.io/doc/latest/html/index.html

[6]The computational times required to perform atomic operations for each method are as follows: ARIMA (2.2 *s*), and ARFIMA (2.1 *s*). These results are obtained using the LC of PG 1553+113. All computations were carried out on a system equipped with an Intel(R) Core(TM) i7-5500U CPU running at 2.40 GHz (dual-core, 4 logical processors) and 16 GB of RAM.

4 CORRECTION AND THE CALIBRATION OF THE TEST STATISTICS

4.1 Global significance

In our periodicity analysis, there was no prior knowledge of the frequencies of the potential signal. In these conditions, it is statistically more rigorous to employ a 'global significance' (e.g. Ait Benkhali et al. 2020). This significance accounts for the look-elsewhere effect, which is the ratio between the probability of observing the excess at some fixed value and the probability of observing it anywhere in the value range considered in the analysis (Gross & Vitells 2010). The 'global significance' is obtained by applying a correction to the 'local significance', which is the test statistics of the periodicity in an LC at a specific value obtained for each method. This correction is approximated by

$$p_{\rm global} = 1 - (1 - p_{\rm local})^N, \quad (3)$$

where N is the trial factor. In our study, we have to consider two potential issues. One is that we do not know the frequency for each source *a priori*, so we must search for the highest peak in each periodogram. The second issue is that we do not know a priori which sources exhibit periodic behaviour, so we must also select them from the periodograms. Consequently, searching P independent periods (frequencies) in each of the periodograms of B blazars, the number of trials is

$$N = P \times B. \quad (4)$$

We do not consider the number of methods in the trials since we present all the results for all the methods equally in our tables for each blazar, avoiding picking the highest significant result according to a single method.

In P20, we analysed ≈2000 blazars; however, after eliminating blazars for which $\geqslant 50$ per cent of the LCs consist of upper limits, the number of blazars included in our sample was 351. There is no unique way to determine P in a given periodogram. For instance, Zechmeister & Kürster (2009) set P based on the frequency range and resolution considered in the periodicity analysis. In our periodograms, we have followed this approach, considering 100 periods (to have a good balance between computational time and resolution in the periodograms). However, for a 12-yr LC with ≈12 samples/year (for approximately $M = 144$ points in the LC), our period range ([1–6] yr) corresponds to 11 independent frequencies sampled. These frequencies are obtained from the expression,

$$f_j = \frac{1}{\delta T} * \frac{j}{M}, \quad (5)$$

where $\delta T = 1/12$ and $j = 1,...,12$, in our case.

A complementary approach to determine P is to perform Monte Carlo simulations (see e.g. Cumming, Marcy & Butler 1999). Following this method, we estimate P by computing the discrete Fourier transforms (DFTs) of 10^8 simulated LCs using the technique of Timmer & Koenig (1995).

The distribution of PSD powers is that of a χ^2 with two degrees of freedom, which can be used to compute the 'local significance' for each PSD. The 'global significance' is computed from the distribution of the highest peak PSD powers for the 10^8 simulated LCs.

To reduce the effects of both red noise leak (transfer of power from low to high frequencies that can conceal a PSD) and aliasing (that can flatten the low-frequency PSD), the LCs are oversampled (Uttley, McHardy & Papadakis 2002) by a factor of 10 (for a total of 1440 time bins). Then, the steps above are repeated for each oversampled PSD, searching it and extracting the power of the highest peak within the 100 frequencies of interest. Finally, we calculate the experimental global and local significance for the over-sampled case (see blue curve in Fig. 1).

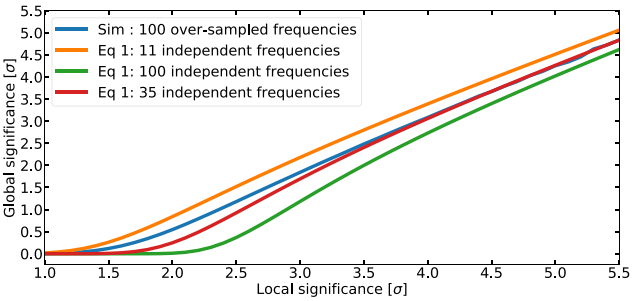

Figure 1. Relation to estimate the number of oversampled frequencies P needed in equation (4) to compute the trial factor. 'equation (1)' denotes the results of applying the equation (3) for a specific number of independent frequencies.

We select the P to correct the 'local significance' $\geq 4\sigma$ to correct precisely the results of the potential high-significance candidates. Fig. 1 shows that adopting $P = 35$ gives the best agreement with the oversampled analysis for the relationship between the 'global significance' and the 'local significance'. Consequently, we choose $P = 35$ for this work, resulting in a trial factor of 12 285 (351×35). The resulting 'global significances' for the high test statistics are:

(i) $\approx 2.8\sigma$ for test statistics of $\approx 5\sigma$
(ii) $\approx 1.8\sigma$ for a test statistics of $\approx 4.5\sigma$
(iii) $< 1\sigma$ for test statistics $< 4.5\sigma$.

To evaluate the influence of P (number of independent frequencies) on the 'global significance', we perform a test. In this test, we fix the B and vary P to observe how it affects the 'global significance'. We use PG 1553+113 as a benchmark, which has a 'local significance' of 4.5σ, corresponding to a 'global significance' of $\approx 1.8\sigma$. The resulting 'global significances' for this'local significance' are:

(i) For $P = 100$, it is $\approx 1.3\sigma$
(ii) For $P = 75$, it is $\approx 1.4\sigma$
(iii) For $P = 50$, it is $\approx 1.6\sigma$
(iv) For $P = 25$, it is $\approx 1.9\sigma$
(v) For $P = 11$, it is $\approx 2.3\sigma$

These results illustrate the role of P in determining the 'global significance'. As P increases, the 'global significance' systematically decreases.

4.2 Power-spectral index estimation

The PSD can be fitted by a power law according to the expression $\propto f^{-\beta}$, where f is the frequency and β is the power-law index (e.g. Gao et al. 2003; Tarnopolski et al. 2020). This form for the PSD denotes that γ-ray variability in blazars is stochastic (e.g. Sobolewska et al. 2014). Additionally, estimates of the power-law index provide information about the nature of the variability, denoting the role of the accretion disk in the emission of the jets (e.g. Bhatta & Dhital 2020).

The power-spectral indices are estimated using the maximum likelihood and MCMC (ML-MCMC)[7]

[7]We use the Python package emcee

The results obtained for the candidates are shown in Table A2. The estimated indices for the power spectrum in most of our candidates are in the range of [0.9–1.5]. This range is compatible with the values proposed in the literature (e.g. Nakagawa & Mori 2013; Sobolewska et al. 2014; Kushwaha et al. 2017; Bhatta & Dhital 2020). However, the obtained indices are ±30 per cent different than those reported by Yang et al. (2021). Ait Benkhali et al. (2020) reported different power spectral indices related to several of our blazars, except for PKS 2155−304 with a compatible $\beta \approx 1$. In Table A2, the mean of the indices for all candidates is ∼1.2 with a standard deviation of 0.4. These indices are compatible with those from Bhatta & Dhital (2020).

We utilize the AIC for each PSD model to evaluate which one provides a more accurate fit. We employ the concept of relative likelihood of models (RLM) to compare the different PSD models. This comparison is conducted by considering a p-value≤ 0.05 and applying the following expression:

$$\exp\left(\frac{\mathrm{AIC_{min}} - \mathrm{AIC}_i}{2}\right) \tag{6}$$

Here, $\mathrm{AIC_{min}}$ represents the minimum AIC value among the models, and AIC_i represents the AIC value of the other model in consideration. As a result, the bending power-law (BPL) model consistently provides a better fit to the PSD in all cases, as shown in Table A2.

Most of the power-law indices shown in Table A2 are consistent with a pink-noise process (spectral index ≈1), which may be caused by disc modulations that materialize as jet modulations. (Bhatta 2022). This process can be associated with short time-scale variability in the periodic baseline (associated with sporadic flaring activity, which might indicate instabilities and turbulence in the accretion flow through the disc or in the jet, Abdo et al. 2010). Additionally, a pink-noise process can be associated with long-term variability coherent on time scales on the order of decades (Bhatta & Dhital 2020). For example, a process that can produce stochastic emission at both short and long timescales is magnetic reconnection (Bhatta & Dhital 2020). In addition to that, variable accretion with large accretion episodes ($\approx$ 50–200 $\mathrm{M_\odot\ yr^{-1}}$) followed by smaller ones can also explain PSDs with indices of ≈1 (Jolley et al. 2009).

Czerny (2004) present a modeling of the relationship between instabilities in the accretion disk and variability, in which the time-scales of these instabilities range from hours to a few years for blazars with BH masses of 10^8–$10^9 \mathrm{M_\odot}$. For instance, these accretion episodes can be associated with a steep power-law index (red noise, with a spectral index ≈2), which produces a dominance of the long-term variability in the LC (e.g. Kunjaya et al. 2011). This scenario may be applicable to PKS 0208−512 (with a power-law index of 1.6 ± 0.4).

Alternatively, Goyal (2018) presents a model to interpret the different timescales observed in the multiwavelength variability of blazars. The variability of the synchrotron emission is powered by a stochastic process with a duration from minutes to years. Regarding the variability of the inverse Compton emission, it results from two stochastic processes, which are linearly overlapping with a duration from one to thousands of days. These two processes are the dissipation in the magnetic field of the jet and inhomogeneities in the number of photons for the inverse-Compton process.

Finally, Rieger (2019, and references therein) propose a model of the dominant radiation processes. Specifically, the power-law index of the PSD depends on the component that dominates the high-energy emission – external Compton or synchrotron self-Compton (with an index of $\gtrsim$ 2.0 signifying the former process).

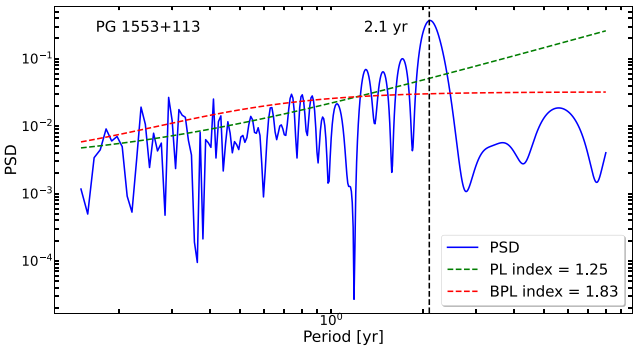

Figure 2. PSD fits for PG 1553+113 according to the PL and BPL approaches.

Furthermore, we employ the ML–MCMC to estimate the index according to the bending power law described in equation (1) (see Fig. 2). The resulting indices are reported in Table A2. The indices are steeper than those reported in the power law case, compatible with the values presented in Gaur et al. (2018).

4.3 Test statistics correction

We also perform a correction to the test statistics of the results of the high-significance candidates denoted by a test statistics $\geq 3\sigma$ (see Section 5.1 and Table A1). This correction is implemented to assess the implications of modifying the assumed PSD models and analysing the influence on the test statistics. We perform this correction to evaluate the effects of changing the assumed PSD (power law and bending power law). We follow the methodology outlined in Section 3.2 to compute the updated test statistics.

In this correction, we use the PSD parameters and their uncertainties of Table A2 obtained with the ML–MCMC method. Specifically for the power law, we consider three different models, combining the PSD indices and normalization values: the index and the normalization minus the corresponding uncertainties, the index and the normalization, and the index and the normalization plus the corresponding uncertainties. Regarding the bending power law, we perform the correction using the PSD indices, the bending frequencies, and normalization values shown in Table A2, with their uncertainties. We also considered three models: index, bending frequency, and normalization minus their corresponding uncertainties; index, bending frequency, and normalization; and index, bending frequency, and normalization plus their corresponding uncertainties.

The results for this correction are shown in Tables A3 and A4. As they show, a ‘redder’ PSD, characterized by a higher power at lower frequencies, leads to reduced significance levels in the detection of long-frequency periods (Ait Benkhali et al. 2020). The methods with the largest corrections are LSP and CWT, while the blazar with the largest corrections is PG 1553+113.

Furthermore, a key distinction between the LSP and the CWT lies in their treatment of time: LSP evaluates the periodic content over the entire time series globally, while CWT provides a time-localized view, capturing how the dominant frequencies vary throughout the observation period. This time-frequency resolution, while beneficial for identifying transient or evolving signals, can also make CWT more sensitive to the variability in the data, such as noise fluctuations or transient events. As a result, the peak frequency identified by CWT may deviate slightly from the true underlying periodicity, producing a broader frequency response and, thus, a lower associated test statistic. These combined factors help explain why CWT tends to yield lower

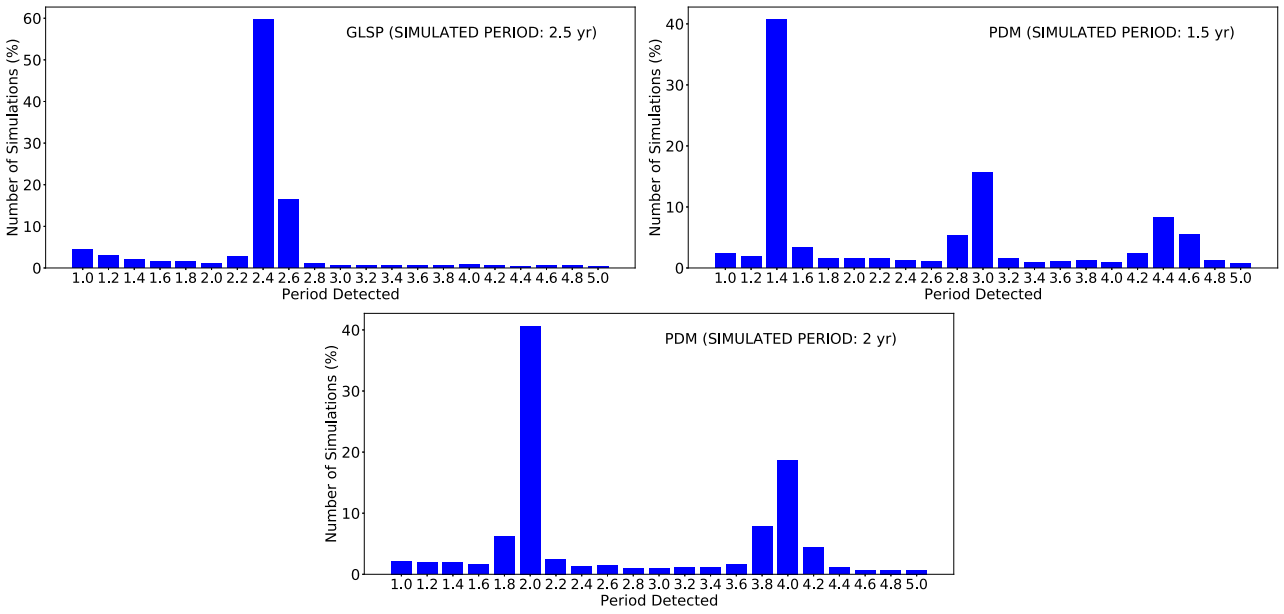

Figure 3. Results of evaluating the false-positive detection rates for the various periodicity-detection methods. *Top*: The results for the GLSP and PDM methods in the case of a sinusoidal LC with periods of 2.5 yr (left) and 1.5 yr (right) that are contaminated with red noise. These results indicate that these methods are robust for periodicity detection against red noise. *Bottom*: The results of the PDM simulations for periods of 2 yr contaminated with red noise. The harmonic effects observed by P20 are also shown.

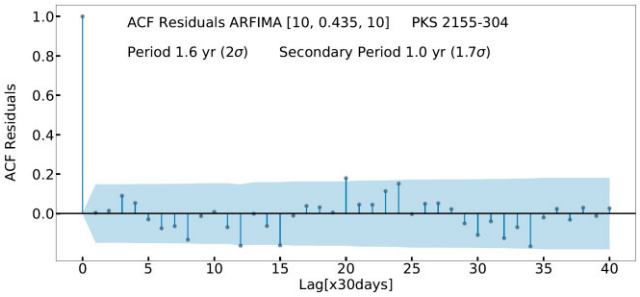

Figure 4. Correlation of the residuals (between the LC and the ARFIMA [p=10, d=0.453, q=10] model) for PKS 2155−204. The coloured area represents the 2σ confidence level. The peak at zero lag represents the autocorrelation of the residual with itself.

significance values compared to LSP in our analysis. This can be observed in Table A1, where in 83 per cent of the cases, CWT results in bigger uncertainty in the period, with 100 per cent of the uncertainty reported by the LSP in 44 per cent of such cases.

4.4 Evaluation of methods against noise

We now evaluate the periodicity detection methods when periodicity is present, but the oscillating fluxes are contaminated by noise (VanderPlas 2018). These methods are LSP, GLSP, PDM, and CWT. We consider four different noises: 'white noise', 'pink noise' (generating random power-law indices in the range [0.8–1.2]), 'red noise' (with power-law indices in the range [1.8 − 2.2]), and 'broken power-law' models.

To implement this scenario, we define a sinusoidal function

$$\phi(t) = O + A \sin\left(\frac{2\pi t}{T} + \theta\right), \tag{7}$$

where the parameters are the offset (O), the amplitude (A), the period (T), and the phase (θ). The offset, amplitude, and phase are randomly selected from the values obtained for each of the 24 candidates from the Markov Chain Monte Carlo sinusoidal fitting method from P20. Specifically, the ranges are [2–15] $\times\ 10^{-8}$ ph cm^{-2} s^{-1} for the offset, [4–40] $\times\ 10^{-8}$ ph cm^{-2} s^{-1} for the amplitude, and [0–2Π] for the phase. We also evaluate any bias in the detection by defining a periodicity range based on the ones from our sample (that is, [1.5–4.5] years). From here, we check if a period is more likely to be detected than others.

We simulate 100 000 sinusoidal LCs for each period-noise combination. Both pink and red noise LCs are produced by applying the Python package `colorednoise`[8], which is based on Timmer & Koenig (1995). The noisy LCs from broken power-law models are generated by the Python package of Connolly (2015), which is derived from Emmanoulopoulos et al. (2013).

The worst results are obtained for white noise and the broken power-law model, with average detection rates of 5 per cent–20 per cent. The method that is the most sensitive to noise is LSP, having the lowest detection rate for all noise patterns. The methods are most robust for fluxes that are contaminated with red noise. In particular, the methods that perform the best are CWT and GLSP, with detection rates of ≈25 per cent–65 per cent (see Fig. 3). Any bias in detecting a specific period is not observed. However, there is a tendency for detection to be more sensitive to noise when the periods are on the higher end of our range, i.e. [3.5–4.5] yr. This is expected since fewer cycles would be included in the data. The exception is pink noise, which results in roughly constant detection rates for all the periods for each method (detection rates ≈12 per cent–17 per cent). Finally, the PDM simulations show the harmonic effects observed in P20. Harmonic effects are only observed when the sinusoidal LCs are contaminated by red noise (see Fig. 3).

[8] https://github.com/felixpatzelt/colorednoise

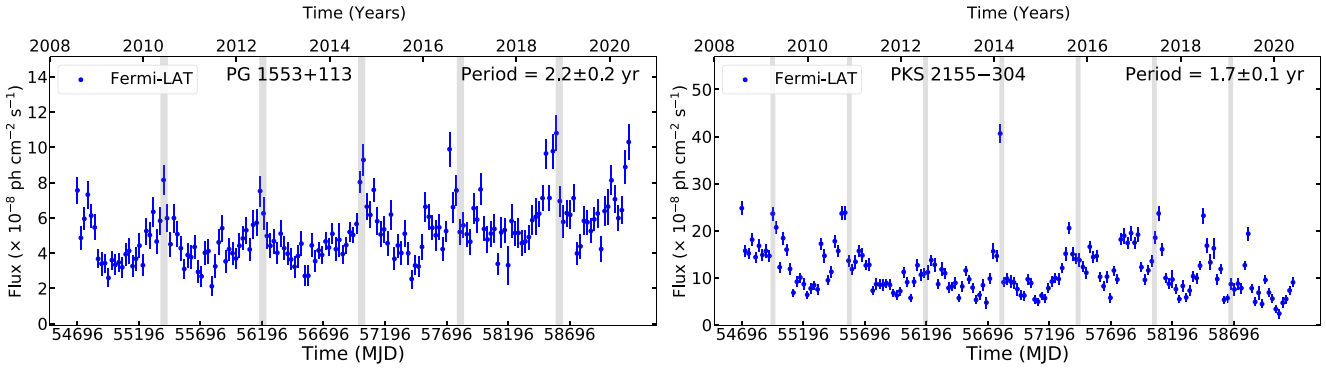

Figure 5. Light curves of the $> 4\sigma$ periodicity sample. The grey vertical bars approximate high-flux periods suggested by the period inferred by the methodology for the given blazar. The width of the grey bars indicates the uncertainty in the periodic signal. Note that it is difficult to identify the periodic emission of S5 0716+714 by eye because this source may have two detected periods (see later).

To further assess the likelihood of false detections, we conduct an additional test aimed at evaluating the spurious detection rate associated with each method. This involves generating 100 000 synthetic LCs following the procedure outlined in Emmanoulopoulos et al. (2013). The resulting period – significance distributions allow us to identify any potential biases toward particular period ranges, which could artificially align with the detected period. This analysis helps determine whether the period – significance pair derived from the original data may arise purely from stochastic variability, leading the method to register a false detection. Additionally, this test also provides a way to estimate the probability that a given periodicity analysis method produces a spurious detection. By quantifying how often similar period-significance combinations appear in purely stochastic data, we can obtain the method's susceptibility to misidentifying noise-induced features as significant periodic signals. We also compute the percentage of cases in which synthetic LCs produce the same period-significance combination as observed in the real data. An occurrence is defined as a case where the recovered period falls within the uncertainty interval of the period found in the original LC, and the associated significance is equal to or higher than that of the original detection. As a reference case, we apply this test to PG 1553+113. The procedure is repeated using both noise models discussed in Section 4.3, the power-law and the bending power-law PSDs.

For the power-law PSD, the detection rates (defined as $\geq 3\sigma$) are as follows: 0.02 per cent for the LSP, 0.31 per cent for the PDM, 0.03 per cent for the GLSP, and 0.01 per cent for the CWT. These values indicate that, under a PL noise assumption, false-positive detections of $\geq 3\sigma$ can still occur with low probability. None of the methods showed any coincidence between the detected period-significance pairs and those obtained from the original data.

When assuming a bending power-law power PSD, the rates of spurious $\geq 3\sigma$ detections are: 0.0 per cent for LSP, 0.2 per cent for PDM, 0.1 per cent for GLSP, and 0.0 per cent for CWT. None of the methods showed any coincidence between the detected period-significance pairs and those obtained from the original data.

Finally, we repeat the test using pure red-noise LCs with a power spectral index of 2. The resulting detection rates are 0.01 per cent for LSP, 0.24 per cent for PDM, 0.02 per cent for GLSP, and 0.0 per cent for CWT, again reinforcing the robustness of the original detections against red-noise contamination.

These results show that the tested methods, LSP, PDM, GLSP, and CWT, are unlikely to yield significant detections from purely stochastic signals. The very low occurrence rates of spurious $\geq 3\sigma$ detections, combined with the zero coincidence of both period and significance with those obtained from real data, suggest that such detections are not easily produced by random fluctuations or artifacts resulting from some bias of the used methods.

5 RESULTS AND DISCUSSION

We run the LCs of our 24 blazars through our improved pipeline. The results of the analysis are listed in Table A1 and Table A5.

To sort the blazars, we quantify the periodicity test statistics by computing the median test statistics across all methods.

5.1 High-significance periodicity candidates

The first group consists of the five blazars with periodicity detections at a median test statistics of $>3\,\sigma$, before the correction described in Section 4.1 is applied. This sample includes 2 sources PG 1553+113 and PKS 2155−304 (Fig. 5). Two different scenarios arise when applying the ARFIMA/ARIMA methods:

(i) The methods find a significant period that is similar (compatible period) to those found via the methods listed in Section 3 and Table A1 (e.g. PKS 2155−304).

(ii) The modeling provides a compatible period at $\geq 1.5\sigma$ (PG 1553+113, the period of $\approx$2 yr for the latter is observed as a secondary peak).

Regarding PG 1553+113 and PKS 2155−304, we confirm our previous period detection (e.g. compatible with Zhang et al. 2017a; Tavani et al. 2018, respectively).

Covino et al. (2018) searched for blazar periodicity in a sample of 10 blazars, including the 2 from our high-significance sample, and they did not find evidence for periodicity. In this case, the different results could be associated with the analysis methodology employed in Covino et al. (2018). Ait Benkhali et al. (2020) also reported mild support for periodicity in some of our high-significance candidates.

Our results are, in general, not consistent with those by Yang et al. (2021, except for PG 1553+113). The reason can be that these authors analyse most of the candidates in P20 using the Continuous-time Autoregressive Moving Average (CARMA). However, according to Feigelson et al. (2018), the CARMA method assumes weak stationary behaviour in LCs without considering any trends in the flux. However, ARFIMA treats such behaviours in the LCs (Feigelson et al. 2018). Yang et al. (2021) justify the use of CARMA on the basis that the LCs they analysed are irregularly

sampled (due to the presence of upper limits). However, moderately irregular measurements can be treated as evenly spaced time series with missing data; hence, the ARIMA/ARFIMA models can also be applied and are better than the CARMA models for analyzing blazar LCs.

In Rico et al. (2024), the same period is obtained for both objects, with local significances of 4.8σ[9] and 4.5σ, for PG 1553+113 and PKS 2155−304, respectively. In this study, a novel method for periodicity analysis is employed: Singular Spectrum Analysis (Greco et al. 2016; Nina Golyandina 2020). This method decomposes the time series into components (oscillatory, trend, and noise), allowing periodicity analysis while mitigating contaminating factors that can distort period search. This approach may explain the difference in local significance inference, as it effectively reduces the impact of distortion factors.

Similarly, in Ren, Cerruti & Sahakyan (2023), a comparable period is identified for both blazars, with local significances of 3.0σ and 2.2σ, respectively. These discrepancies in local significance may arise from differences in the methodologies used to estimate them. Specifically, in Ren et al. (2023), the PSD is modelled with a smooth bending power-law plus white noise, as described in Vaughan (2010). However, the paper does not present the parameters and plots for each PSD fit, preventing a direct comparison with our estimations.

5.2 Low-significance periodicity candidates

The rest of the sample includes 9 blazars with periods detected at $\geqslant 2\sigma$ (OJ 014, PKS 0454−234, S5 0716+714, GB6 J0043+3426, TXS 0518+211, 87GB 164812.2+524023, PKS 0447–439, PKS 0426−380, PKS 0301−243; see Table 1 and Fig. A1). We discard 13 candidates with a median test statistics of $< 2.0\sigma$ (S4 1144+40, PG 1246+586, PKS 0250−225, PKS 2255−282, TXS 1902+556, S3 0458−02, MG2 J130304+2434, PKS 2052−47, S4 0814+42, MG1 J021114+1051, TXS 0059+581, TXS 1452+516, PKS 0208−512).

The periods of the blazars presented previously in the literature are mostly compatible with our corresponding results (e.g. PKS 0426−380 and MG2 J130304+2434, Zhang et al. 2017b, c, respectively). In the case of S5 0716+714, excluding the ARFIMA/ARIMA analysis, we confirm the period of ≈2.7 yr found in P20 and in the recent analysis by Bhatta (2021). This period differs from the ≈ 0.9 yr period reported by Prokhorov & Moraghan (2017), Li et al. (2018), Sandrinelli et al. (2017), and Bhatta & Dhital (2020). However, we report the ≈0.9 yr period as a secondary peak (see Table A1). These disagreements may be due to the fact that we use more telescope time (e.g. ∼8 yr in Li et al. 2018; Bhatta & Dhital 2020) or by the technique employed to infer test statistics (e.g. Prokhorov & Moraghan 2017; Bhatta & Dhital 2020). For PKS 0454−234, Bhatta & Dhital (2020) do not find any significant detection (note that we use more telescope time, and the test statistics is obtained differently).

In general, Rico et al. (2024) reported a higher local significance for the previously studied objects, namely 4.8σ for OJ 014 and TXS 0518+211. This increased significance is attributed to the analysis of a 'clean' LC free of potential distorting factors.

We note that not all of the candidates presented by P20 increased the test statistics with the additional 3 yr of data. For example, large drops in test statistics were found for TXS 0059+581, TXS 1452+516 or PKS 0208−512 (see Table 1). This fact might indicate that the inferred period could not be genuine (e.g. Liu, Gezari & Miller 2018).

This reduction of significance with more years could be due to different factors. For instance, the flare at the end of the LC of PKS 0208−512 affects the periodicity analysis. A flare adds a strong non-periodic feature to the LC, increasing the overall variability and introducing additional power across a broad range of frequencies. This distorts the periodogram and can obscure the previously detected periodic signal. As a result, the coherence of the signal weakens, and its statistical significance decreases. This scenario could also apply to TXS 0059+581. Although the flare was present in the 9-yr LC, with the extra years, it could be more evident that the modulation is not sustained, and the signal is likely dominated by transient variability rather than a persistent periodic process. Consequently, the extension of the time baseline reveals that the previously obtained periodicity may have been biased by the episodic presence of the flare, rather than reflecting a stable periodic pattern.

In other scenarios (i.e. PG 1246+586, TXS 1452+516), the addition of three years of data can contribute to diluting the apparent coherence of the signal. This results in a higher dominance of red noise. As the baseline increases, low-frequency fluctuations inherent to red noise gain more statistical weight, often reducing the contrast between a potential periodic signal and stochastic variability. Consequently, the test statistics of the obtained period decrease as the signal becomes less distinguishable from the background noise structure.

5.3 Lower energy counterparts

For some of the blazars in our sample, ∼year-long periods have previously been reported at lower energies. In this section, we review an incomplete segment of the relevant literature, primarily focusing on PG 1553+113 and PKS 2155−304, which arguably are the most popular and promising candidates. Covino et al. (2020) also summarize studies that have reported periodic LCs for PG 1553+113 and PKS 2155−304 in γ-ray and optical bands. Another recent discussion on the optical emission of PKS 2155−304 and S5 0716+714 can be found in section 3.3.1 of Bhatta & Dhital (2020).

Ackermann et al. (2015) first identified a ≈ 2.1 yr periodicity in the optical, radio, and γ-ray bands for PG 1553+113. Their 2.1 yr period agrees with our results. A later study by Covino et al. (2020) used Gaussian process modelling and a longer temporal baseline to search for periodicity in PG 1553+113. This study found that the quality of the fit in both the optical and γ-ray bands can be improved by including a component with a similar period to the one found in our results (≈ 2.2 yr).

To our knowledge, the first positive identification of ∼year-long periods for PKS 2155−304 was found in the optical band by Fan & Lin (2000). The periods they reported were approximately 4.2 and 7 yr. A later study by Zhang et al. (2014) used a much longer temporal baseline for analyzing optical data but did not recover these multiyear periods as primary periodicities. Instead, Zhang et al. (2014) reported a period of ≈ 0.87 yr, and suggested that the 4.2 and 7 yr periods reported by Fan & Lin (2000) may be respectively 4th and 7th harmonics of the primary 0.87 yr period. The optical periodicity of ≈ 0.87 yr for PKS 2155−304 is approximately half of the γ-ray periodicity of ≈ 1.7 yr that we report in this work. Sandrinelli, Covino & Treves (2014) also reported a detection of the ≈ 0.87 yr periodicity in the optical band, as well as a tentative detection of a ∼year-long periodicity (similar to the ≈ 1.7 yr periodicity in γ-rays that we report here). Their findings were reiterated in Sandrinelli et al. (2016). There is some indication of the 0.87 yr period in Fig.

[9]The maximum significance to be obtained according to the number of artificial LCs used to estimate it.

2 of the publication by Covino et al. (2020), but that period was not the focus of their work. Covino et al. (2020) explain the seemingly discrepant periodicity measurements for PKS 2155−304 as possibly arising from differences in the noise models considered in the data analysis.

There are indications from some studies of consistent periodicities in the optical and γ-ray bands. For example, a recent analysis by Bhatta (2021) found similar periods in the optical and γ-ray bands for two of our high-significance sources: ≈ 1.7 yr for PKS 2155−304 and ≈ 2.7 yr for S5 0716+714. In particular, they did not find evidence for the 0.87 yr optical period for PKS 2155−304 reported in Zhang et al. (2014). They argued that consistent periods in different bands are evidence of the periodicity being genuine.

6 PERIODICITY INTERPRETATION

A variety of scenarios have been proposed in the literature to explain periodic emissions in blazars. Possible interpretations of long-term periodicity can be grouped into two categories: (1) periodicity in single black hole systems and (2) periodicity in binary black hole systems.

6.1 Periodicity in single black hole systems

In the first category, the emission mechanism is interpreted in the context of a single-SMBH system, where the periodic emission is produced by modulations in the accretion flow or by jet precession. For example, Mohan & Mangalam (2015) propose a scenario in which plasma inhomogeneities from the accretion disc propagate into the jet and generate periodic emission due to helical motions along magnetic surfaces within the jet. In models proposed in Villata & Raiteri (1999) and Ostorero, Villata & Raiteri (2004), the precession of the jet axis induces periodic variation in the line-of-sight emission.

Alternatively, periodicity could emerge from the overall modulation of the accretion power, which is (sensibly) assumed to be reflected in the jet power. Gracia et al. (2003) invoked such scenario for the periodicity of PKS 2155−304 (see H. E. S. S. Collaboration 2017). The lognormal shape of the flux PDF suggests an underlying multiplicative process (e.g. Shah et al. 2018); as such, it favours an accretion-disc origin for the periodicity over an additive process such as jets-in-jet (e.g. Uttley, McHardy & Vaughan 2005; Rieger 2019). Since accretion disks in the vicinity of SMBHs are expected to be dominated by radiation pressure, they are subject to a variety of instabilities (Lightman & Eardley 1974), which can lead to limit-cycle behaviour that conceivably appears as quasi-periodic emission over a few cycles (Frank, King & Raine 2002). Recent 3-dimensional simulations of a single SMBH give a concrete example of opacity-driven light curve variability lasting for 2–6 cycles, encompassing a span of years to decades (Jiang & Blaes 2020). Over a few cycles, such variability may appear to be quasi-periodic.

6.2 Periodicity in binary black hole systems

The second category of proposed mechanisms invokes an SMBHB. There are two variations of this scenario: (i) perturbations caused by the secondary SMBH destabilize the accretion flow of the primary SMBH, modulating the accretion rate and, as a consequence, the luminosity of the blazar (Sandrinelli et al. 2016); (ii) the periodic emission may be due to jet precession, ultimately caused by the orbiting SMBHs (Sobacchi, Sormani & Stamerra 2017). The SMBHB hypothesis has been applied to explain the LC of PG 1553+113 (e.g. Cavaliere, Tavani & Vittorini 2017; Sobacchi et al. 2017; Tavani et al. 2018).

Major galaxy mergers are found more frequently at a moderate redshift of about $z \sim 1$ when galaxies are also more gas-rich (e.g. Tacconi et al. 2010; Koss et al. 2018). In turn, the number of SMBHBs should increase with increasing redshift and increasing mass (Volonteri, Miller & Dotti 2009). Most of our candidates reside at redshifts $z \gtrsim 1$ (see Table 1).

In order to discriminate between different hypotheses, the periodicity search may be complemented by spectroscopy. Two different approaches can be useful to infer the presence of an SMBHB by using optical emission lines: radial velocity shifts and line shapes. Regarding radial velocity shifts, the lines are expected to oscillate about their rest-frame wavelength on the time scale corresponding to the orbital period (e.g. Liu et al. 2014,, typically one targets the Hβ and MgII lines). The other technique to infer close binary systems is to observe double-peaked profiles in the emission lines (e.g. Hβ, Kovačević, Wang & Popović 2020).

6.3 Application of the binary hypothesis to PG 1553+113 and PKS 2155−304

Here, we discuss the application of the binary hypothesis to two blazars in our sample with the highest-significance periodicity: PG 1553+113 and PKS 2155−304. These candidates are arguably the most promising because they are bright and have the greatest number of cycles (≈ 6 for PG 1553+113, ≈ 7 for PKS 2155−304), and our autoregression analysis (ARFIMA/ARIMA) reports compatible periods with the methods of Table A5.

Covino et al. (2020) used Gaussian processes to analyse data from optical and previous *Fermi*-LAT observations. They found that adding a periodic component increased the statistical quality of fit for both candidates PG 1553+113 and PKS 2155−304 (although it is less convincing for PG 1553+113). A large number of cycles also helps in addressing the concerns raised by Vaughan et al. (2016) regarding spurious periodicity in LCs with only a few putative periods present. Also, note that the test statistics we report has increased with the addition of 3 yr of data; in contrast, adding new data for quasar PG 1302−102 resulted in a decrease in test statistics for the periodicity, which was seen as evidence against the authenticity of the periodicity (Liu et al. 2018). The idea was that if the periodicity were genuine, one would generally expect the test statistics of the detected period to become larger with new data. We note that the latest upper bound on the binary fraction of blazars from the Pulsar Timing Array (at most $\approx 1/1000$ blazars host binaries with orbital periods less than 5 years, Holgado et al. 2018) is compatible with the presence of few true SMBHBs in the *Fermi*-LAT catalog (Holgado et al. 2018).

For PKS 2155−304, there is a disparity in the mass estimates for the SMBH. The $M_{\rm BH} - L_{\rm bulge}$ relation suggests a central black hole mass of $M_{\rm BH} \gtrsim 2 \times 10^8 {\rm M}_\odot$. On the other hand, VHE variability on time scales of $\lesssim$200 s suggest a black hole mass of $M_{\rm BH} \lesssim 4 \times 10^7\ {\rm M}_\odot$ (Rieger & Volpe 2010). Variability in the X-ray band supports a lower mass estimate (Hayashida et al. 1998; Czerny et al. 2001). Rieger & Volpe (2010) argued that the discrepancy in mass estimates could be explained if PKS 2155−304 hosts an SMBHB: the $M_{\rm BH} - L_{\rm bulge}$ relation measures the binary mass while the fast variability reflects the mass of the secondary SMBH. This scenario requires that the jet emission comes mostly from the secondary SMBH, which is *prima facie* consistent with recent simulations of accreting unequal-mass binaries (Duffell et al. 2020). These simulations show that the secondary can accrete as much as 10× faster than the primary.

The different mass estimates constitute a bound on the SMBHB mass ratio$-q \lesssim 0.2$, which implies that the secondary accretes at ≈ 3–$10\times$ the rate of the primary (as seen in the simulations of Duffell et al. 2020). However, the physics of jet launching is rather complicated and not fully understood, so caution is warranted with circumstantial evidence such as this. Caution is also warranted when applying 2-dimensional thin-disk simulation results such as from Duffell et al. (2020), since that set-up uses a variety of approximations. We refer to Rieger (2019) and references therein for a recent overview of the binary hypothesis for PKS 2155−304. Attempts to explain the short time-scale variability without a binary are given in Begelman, Fabian & Rees (2008) and Levinson (2007).

For PG 1553+113, variability on a 2400-s time-scale leads to an SMBH mass estimate of $M_{\rm BH} \approx 4 \times 10^7$–$8 \times 10^8 {\rm M}_\odot$, depending on the black hole's spin (with higher spins implying larger masses Dhiman et al. 2021). However, an estimate based on the $M_{\rm BH}$–$L_{\rm bulge}$ relation is not possible because the host galaxy has not yet been identified. As a basis for discussion, let us consider the orbital parameters from the binary model proposed by Cavaliere et al. (2017): primary SMBH mass $5 \times 10^8 M_\odot$, mass ratio $q = 0.1$, eccentricity $e \approx 0.2$. In the model, mild non-zero eccentricity is required for the secondary SMBH to perturb the presumed jet from the primary SMBH on the orbital time-scale. Thin-disc simulations find two values of the eccentricity that are stable under gas-driven binary evolution, $e = 0$ (circular) and $e \approx 0.45$ (D'Orazio & Duffell 2021; Zrake et al. 2021). Thus, one may infer that the $e = 0.2$ binary has been circularizing for some time due to gravitational wave emission. Consistency then requires that the evolution of the binary is already dominated by the emission of gravitational waves (i.e. the orbital radius is less than the 'gas decoupling' orbital radius). Let the binary semi-major axis be a and its total mass be M. We can estimate the orbital period when gas-driven evolution is on par with gravitational wave-driven evolution by assuming post-Newtonian orbital evolution (Peters 1964) and using $\mathrm{d}\log a/\mathrm{d}\log M = -l$. l is the 'accretion eigenvalue', which determines the rate at which the binary semi-major axis evolves (and whether the binary is expanding or shrinking). Here, $l \sim \mathcal{O}(1)$ is determined by gas-accretion physics from thin-disc simulations. In following this procedure, we can set a, the rate of gas-driven evolution, to that of the gravitational-wave – driven evolution and solve for the orbital period. A positive value of l corresponds to a gas-driven inspiral, which is reasonable for large disc Mach numbers ($\gtrsim 25$; Tiede et al. 2020) typically expected in AGN diss. Let us consider an accretion rate equal to the Eddington limit (assuming a typical efficiency of $\epsilon = 0.1$). Even if we use a very large value $l = 10$ (which results in a shorter orbital period at decoupling), we find that the orbital period at decoupling is nearly 6 yr. Thus, under these standard assumptions, the proposed binary seems to have transitioned into the gravitational wave-driven regime with an orbital period of ≈ 1.5 yr (in the source frame). It would be interesting to carefully compute the orbital evolution history to see whether the proposed eccentricity of $e = 0.2$ at the current orbital separation is consistent with the equilibrium value prior to the time of decoupling.

Lastly, simulations of accreting binaries have generally shown two possible main periodicities in accretion rates−that of the binary's orbital period, $T_{\rm binary}$, and that of an overdensity (called a 'lump') orbiting at larger radii with a period $\approx (5-10) \times T_{\rm binary}$. The lump period is expected to dominate for mass ratios $q \gtrsim 0.2$ (D'Orazio, Haiman & MacFadyen 2013; Farris et al. 2014; Duffell et al. 2020) and eccentricities $e \lesssim 0.1$ (Miranda, Muñoz & Lai 2016; Zrake et al. 2021). If the periodic LCs revealed in this study correspond to the lump period in a circumbinary disc, then the SMBHBs are orbiting faster and are thus closer to merging. Future measurements of gravitational waves from SMBHBs could reveal whether the electromagnetic emission is being modulated by the lump or the binary orbital period (D'Orazio et al. 2015).

7 SUMMARY

In this work, we analyse the γ-ray LCs of the most promising 24 periodicity candidates presented by P20. Relative to P20, these LCs are extended from 9 to 12 yr of *Fermi*-LAT data and the energies are expanded from >1 to >0.1 GeV, increasing the signal-to-noise ratio. In addition, the upper limits are treated in a way that allows us to retain information about the flux variations. We also employ an improved version of our periodicity-search pipeline, composed of seven different methods to infer periods and the associated test statistics. This pipeline is improved by including the ARIMA/ARFIMA autoregressive algorithm. As a result, we have obtained that 1553+113 with periodic γ-ray emission detected at a 'global significance' level of $\approx 1.8\sigma$.

8 SOFTWARE

(i) ARFIMA R-software (Hyndman & Khandakar 2008; Hyndman et al. 2024),
(ii) ASTROML (Ivezić et al. 2014),
(iii) ASTROPY (Astropy Collaboration 2013, 2018, 2022),
(iv) COLOREDNOISE https://github.com/felixpatzelt/colorednoise,
(v) EMCEE (Foreman-Mackey et al. 2013),
(vi) FERMIPY software package (Wood et al. 2017),
(vii) PYASTRONOMY (Czesla et al. 2019),
(viii) PYCWT[10] https://pypi.org/project/pycwt/,
(ix) rpy2 https://rpy2.github.io/doc/latest/html/index.html,
(x) stats R-software (R Core Team 2024),
(xi) statsmodels (Skipper Seabold & Josef Perktold 2010),
(xii) SCIPY (Virtanen et al. 2020),
(xiii) Simulating light curves (Connolly 2015),

ACKNOWLEDGEMENTS

The *Fermi*-LAT Collaboration acknowledges generous ongoing support from a number of agencies and institutes that have supported both the development and the operation of the LAT as well as scientific data analysis. These include the National Aeronautics and Space Administration and the Department of Energy in the United States, the Commissariat à l'Energie Atomique and the Centre National de la Recherche Scientifique/Institut National de Physique Nucléaire et de Physique des Particules in France, the Agenzia Spaziale Italiana and the Istituto Nazionale di Fisica Nucleare in Italy, the Ministry of Education,Culture, Sports, Science and Technology (MEXT), High Energy Accelerator Research Organization (KEK) and Japan Aerospace Exploration Agency (JAXA) in Japan, and the K. A. Wallenberg Foundation, the Swedish Research Council and the Swedish National Space Board in Sweden.

Additional support for science analysis during the operations phase is gratefully acknowledged from the Istituto Nazionale di Astrofisica in Italy and the Centre National d'Études Spatiales in France. This work was performed in part under DOE Contract DE-AC02-76SF00515.

[10]We have modified the sources of the code to estimate the test statistics with Connolly (2015)

PP and MA acknowledge funding under NASA contract 80NSSC20K1562. SB acknowledges financial support by the European Research Council for the ERC Starting grant MessMapp, under contract no. 949555, and by the German Science Foundation DFG, research grant 'Relativistic Jets in Active Galaxies' (FOR 5195, grant no. 443220636). AD is thankful for the support of the Ramón y Cajal program from the Spanish MINECO, Proyecto PID2021-126536OA-I00 funded by MCIN/AEI/10.13039/501100011033, and Proyecto PR44/21-29915 funded by the Santander Bank and Universidad Complutense de Madrid.

This work was supported by the European Research Council, ERC Starting grant *MessMapp*, SB Principal Investigator, under contract no. 949555, and by the German Science Foundation DFG, research grant 'Relativistic Jets in Active Galaxies' (FOR 5195, grant no. 443220636).

Finally, the authors acknowledge S. Fegan for useful discussions, which helped to improve the paper.

DATA AVAILABILITY

All the data used in this work are publicly available or available on request to the responsible for the corresponding observatory/facility.

REFERENCES

Abdo A. A. et al., 2010, ApJ, 722, 520
Abdollahi S. et al., 2020, ApJS, 247, 33
Abdollahi S. et al., 2022, ApJS, 260, 53
Ackermann M. et al., 2015, ApJ, 813, L41
Ait Benkhali F., Hofmann W., Rieger F. M., Chakraborty N., 2020, A&A, 634, A120
Akaike H., 1973, Biometrika, 60, 255
Astropy Collaboration et al., 2013, A&A, 558, A33
Astropy Collaboration et al., 2018, AJ, 156, 123
Astropy Collaboration et al., 2022, ApJ, 935, 167
Atwood W. et al., 2009, ApJ, 697, 1071
Atwood W. et al., 2013, preprint (arXiv:1303.3514)
Baillie R. T., 1996, J. Econometrics, 73, 5
Ballet J., Burnett T. H., Digel S. W., Lott B., 2020, preprint (arXiv:2005.11208)
Begelman M. C., Blandford R. D., Rees M. J., 1980, Nature, 287, 307
Begelman M. C., Fabian A. C., Rees M. J., 2008, MNRAS, 384, L19
Bhatta G., 2021, ApJ, 923, 7
Bhatta G., 2022, preprint (arXiv:2204.08923)
Bhatta G., Dhital N., 2020, ApJ, 891, 120
Bruel P., Burnett T. H., Digel S. W., Johannesson G., Omodei N., Wood M., 2018, preprint (arXiv:1810.11394)
Caceres G. A., Feigelson E. D., Babu G. J., Bahamonde N., Christen A., Bertin K., Meza C., Curé M., 2019, AJ, 158, 57
Cavaliere A., Padovani P., 1989, ApJ, 340, L5
Cavaliere A., Tavani M., Vittorini V., 2017, ApJ, 836, 220
Chakraborty N., Rieger F. M., 2020, preprint (arXiv:2010.01038)
Chatfield C., 2004, The analysis of time series: an introduction, 6thedn. CRC Press, Florida, US
Colpi M., 2014, Space Sci. Rev., 183, 189
Connolly S. D., 2015, preprint (arXiv:1503.06676)
Covino S., Sandrinelli A., Treves A., 2018, MNRAS, 482, 1270
Covino S., Landoni M., Sandrinelli A., Treves A., 2020, ApJ, 895, 122
Cumming A., Marcy G. W., Butler R. P., 1999, ApJ, 526, 890
Czerny B., 2004, preprint(astro–ph/0409254)
Czerny B., Nikołajuk M., Piasecki M., Kuraszkiewicz J., 2001, MNRAS, 325, 865
Czesla S., Schröter S., Schneider C. P., Huber K. F., Pfeifer F., Andreasen D. T., Zechmeister M., 2019, Astrophysics Source Code Library, record ascl:1906.010
D'Orazio D. J., Duffell P. C., 2021, ApJ, 914, L21
D'Orazio D. J., Haiman Z., MacFadyen A., 2013, MNRAS, 436, 2997
D'Orazio D. J., Haiman Z., Duffell P., Farris B. D., MacFadyen A. I., 2015, MNRAS, 452, 2540
Dhiman V., Gupta A. C., Gaur H., Wiita P. J., 2021, MNRAS, 506, 1198
Dickey D. A., Fuller W. A., 1979, J. Am. Stat. Assoc., 74, 427
Dosopoulou F., Antonini F., 2017, ApJ, 840, 31
Duffell P. C., D'Orazio D., Derdzinski A., Haiman Z., MacFadyen A., Rosen A. L., Zrake J., 2020, ApJ, 901, 25
Emmanoulopoulos D., McHardy I. M., Papadakis I. E., 2013, MNRAS, 433, 907
Enoki M., Inoue K. T., Nagashima M., Sugiyama N., 2004, ApJ, 615, 19
Fan J. H., Lin R. G., 2000, A&A, 355, 880
Farris B. D., Duffell P., MacFadyen A. I., Haiman Z., 2014, ApJ, 783, 134
Feigelson E. D., Babu G. J., Caceres G. A., 2018, Front. Phys., 6, 80
Foreman-Mackey D., Hogg D. W., Lang D., Goodman J., 2013, PASP, 125, 306
Foster G., 1996, AJ, 112, 1709
Frank J., King A., Raine D. J., 2002, Accretion Power in Astrophysics: Third Edition Cambridge University Press, Cambridge, UK
Gao J. B., Cao Y., Lee J.-M., 2003, Phys. Lett. A, 314, 392
Gaur H., Mohan P., Wierzcholska A., Gu M., 2018, MNRAS, 473, 3638
Goyal A., 2018, Galaxies, 6, 34
Goyal A. et al., 2017, ApJ, 837, 127
Gracia J., Peitz J., Keller C., Camenzind M., 2003, MNRAS, 344, 468
Greco G. et al., 2016, in Napolitano N. R., Longo G., Marconi M., Paolillo M., Iodice E., eds, Astrophys. Space Sci. Proc. Vol. 42, The Universe of Digital Sky Surveys. Springer, Switzerland, p. 105
Gross E., Vitells O., 2010, Euro. Phys. J. C, 70, 525
H. E. S. S. Collaboration 2017, A&A, 598, A39
Haiman Z., Kocsis B., Menou K., 2009, ApJ, 700, 1952
Häring N., Rix H.-W., 2004, ApJ, 604, L89
Hayashida K., Miyamoto S., Kitamoto S., Negoro H., Inoue H., 1998, ApJ, 500, 642
Holgado A. M., Sesana A., Sandrinelli A., Covino S., Treves A., Liu X., Ricker P., 2018, MNRAS, 481, L74
Hyndman R. J., Khandakar Y., 2008, J. Stat. Softw., 27, 1
Hyndman R. et al., 2024, forecast: Forecasting functions for time series and linear models. https://pkg.robjhyndman.com/forecast/
Ivezić Z., Connolly A. J., VanderPlas J. T., Gray A., 2014, Statistics, Data Mining, and Machine Learning in Astronomy: A Practical Python Guide for the Analysis of Survey Data. Princeton Univ. Press, New Jersey
Jiang Y.-F., Blaes O., 2020, ApJ, 900, 25
Jiang T., Hogg D. W., Blanton M. R., 2012, ApJ, 759, 140
Jolley E. J. D., Kuncic Z., Bicknell G. V., Wagner S., 2009, MNRAS, 400, 1521
Koss M. J. et al., 2018, Nature, 563, 214
Kovačević A. B., Wang J.-M., Popović L. Č., 2020, A&A, 635, A1
Kunjaya C., Mahasena P., Vierdayanti K., Herlie S., 2011, Ap&SS, 336, 455
Kushwaha P., Sinha A., Misra R., Singh K. P., de Gouveia Dal Pino E. M., 2017, ApJ, 849, 138
Levinson A., 2007, ApJ, 671, L29
Li X.-P., Luo Y.-H., Yang H.-Y., Yang C., Cai Y., Yang H.-T., Zhou L., Shan Y.-Q., 2018, Ap&SS, 363, 169
Lightman A. P., Eardley D. M., 1974, ApJ, 187, L1
Lin L. et al., 2008, ApJ, 681, 232
Linnell Nemec A., Nemec J. M., 1985, AJ, 90, 2317
Liu X., Shen Y., Bian F., Loeb A., Tremaine S., 2014, ApJ, 789, 140
Liu T., Gezari S., Miller M. C., 2018, ApJ, 859, L12
Ljung G. M., Box G. E. P., 1978, Biometrika, 65, 297
Lomb N. R., 1976, Ap&SS, 39, 447
Mattox J. R. et al., 1996, ApJ, 461, 396
Miranda R., Muñoz D. J., Lai D., 2016, MNRAS, 466, 1170
Mohan P., Mangalam A., 2015, ApJ, 805, 91
Nakagawa K., Mori M., 2013, ApJ, 773, 177
Nina Golyandina A. Z., 2020, Singular Spectrum Analysis for Time Series, 2 edn. S, Springer Berlin, Heidelberghttps://doi.org/10.1007/978-3-662-62436-4

Ostorero L., Villata M., Raiteri C. M., 2004, A&A, 419, 913
Peñil P. et al., 2020, ApJ, 896, 134
Peñil P., Domínguez A., Buson S., Ajello M., Adhikari S., Rico A., 2025, ApJ, 980, 38
Peters P. C., 1964, Phys. Rev., 136, B1224
Prokhorov D. A., Moraghan A., 2017, MNRAS, 471, 3036
R Core Team, 2024, R: A Language and Environment for Statistical Computing. R Foundation for Statistical Computing, Vienna, Austria, https://www.R-project.org/
Ren H. X., Cerruti M., Sahakyan N., 2023, A&A, 672, A86
Rico A., Domínguez A., Peñil P., Ajello M., Buson S., Adhikari S., Movahedifar M., 2024, A&A, 697, 24
Rieger F. M., 2007, Ap&SS, 309, 271
Rieger F. M., 2019, Galaxies, 7, 28
Rieger F. M., Volpe F., 2010, A&A, 520, A23
Sandrinelli A., Covino S., Treves A., 2014, ApJ, 793, L1
Sandrinelli A., Covino S., Dotti M., Treves A., 2016, AJ, 151, 54
Sandrinelli A. et al., 2017, A&A, 600, A132
Scargle J. D., 1981, ApJS, 45, 1
Scargle J. D., 1982, ApJ, 263, 835
Schulz M., Mudelsee M., 2002, Comput. Geosci., 28, 421
Seabold S., Perktold J, 2010, in van der Walt S., Millman J., eds, Proceedings of the 9th Python in Science Conference. Austin, Texas, USA, p. 92
Shah Z., Mankuzhiyil N., Sinha A., Misra R., Sahayanathan S., Iqbal N., 2018, Res. Astron. Astrophys., 18, 141
Shah Z., Misra R., Sinha A., 2020, MNRAS, 496, 3348
Sobacchi E., Sormani M. C., Stamerra A., 2017, MNRAS, 465, 161
Sobolewska M. A., Siemiginowska A., Kelly B. C., Nalewajko K., 2014, ApJ, 786, 143
Soltan A., 1982, MNRAS, 200, 115
Stellingwerf R. F., 1978, ApJ, 224, 953
Tacconi L. J. et al., 2010, Nature, 463, 781
Tarnopolski M., Żywucka N., Marchenko V., Pascual-Granado J., 2020, ApJS, 250, 1
Tavani M., Cavaliere A., Munar-Adrover P., Argan A., 2018, ApJ, 854, 11
Tiede C., Zrake J., MacFadyen A., Haiman Z., 2020, ApJ, 900, 43
Timmer J., Koenig M., 1995, A&A, 300, 707
Torrence C., Compo G. P., 1998, Bull. Am. Meteorol. Soc., 79, 61
Urry C. M., 1996, in Miller H. R., Webb J. R., Noble J. C., eds, ASP Conf. Ser. Vol. 110, Blazar Continuum Variability. Astron. Soc. Pac., San Francisco, p. 391
Urry M., 2011, JA&A, 32, 139
Uttley P., McHardy I. M., Papadakis I. E., 2002, MNRAS, 332, 231
Uttley P., McHardy I. M., Vaughan S., 2005, MNRAS, 359, 345
Valtonen M. J. et al., 2016, ApJ, 819, L37
VanderPlas J. T., 2018, ApJS, 236, 16
Vaughan S., 2005, A&A, 431, 391
Vaughan S., 2010, MNRAS, 402, 307
Vaughan S., Uttley P., Markowitz A., Huppenkothen D., Middleton M., Alston W., Scargle J., Farr W., 2016, MNRAS, 461, 3145
Villata M., Raiteri C. M., 1999, A&A, 347, 30
Virtanen P. et al., 2020, Nat. methods, 17, 261
Volonteri M., Miller J. M., Dotti M., 2009, ApJ, 703, L86
Wiita P. J., 2006, preprint(astro–ph/0603728)
Wood M., Caputo R., Charles E., Di Mauro M., Magill J., Perkins J. S., Fermi-LAT Collaboration, 2017, 35th International Cosmic Ray Conference (ICRC2017), Busan, South Korea, p. 824(arXiv:1707.09551)
Xu C., 2019, AJ, 157, 127
Yang S., Yan D., Zhang P., Dai B., Zhang L., 2021, ApJ, 907, 105
Zechmeister M., Kürster M., 2009, A&A, 496, 577
Zhang B.-K., Zhao X.-Y., Wang C.-X., Dai B.-Z., 2014, Res. Astron. Astrophys., 14, 933
Zhang P.-f., Yan D.-h., Liao N.-h., Wang J.-c., 2017a, ApJ, 835, 260
Zhang P.-f., Yan D.-h., Liao N.-h., Zeng W., Wang J.-c., Cao L.-J., 2017b, ApJ, 842, 10
Zhang P.-F., Yan D.-H., Zhou J.-N., Fan Y.-Z., Wang J.-C., Zhang L., 2017c, ApJ, 845, 82
Zhang P.-f., Yan D.-h., Zhou J.-n., Wang J.-c., Zhang L., 2020, ApJ, 891, 163
Zrake J., Tiede C., MacFadyen A., Haiman Z., 2021, ApJ, 909, L13

APPENDIX A: APPENDIX

A1 Light curves

Fig. A1 reports the LCs of the low-significance blazars.

A2 Power spectral densities

Fig. A2 reports the PSD plots of the blazars in Table A2.

A3 Tables

This section presents Tables A2, A3, A1, and A5, which summarize the various estimations used to determine the periods of the selected blazars.

Table A1. List of periods and uncertainties (top) with their associated test statistics (bottom) for the periodic-emission candidates following a similar structure as Table 1. Note that there are some sources with two periods with high test statistics (organized by the amplitude of the peak), which are denoted by ⋆. The symbol † denotes the PDM results that present the harmonic effect described in Peñil et al. (2020). The symbol ‡ denotes periods that were presented in the CWT for 12 yr of LC data. All periods are in years.

Association Name	LSP	GLSP	PDM	CWT
PG 1553+113	$2.1^{\pm0.2}_{5.1\sigma}$	$2.1^{\pm0.2}_{4.6\sigma}$	$2.2^{\pm0.1}_{4.2\sigma}$	$‡2.2^{\pm0.4}_{4.4\sigma}$
PKS 2155−304	$1.7^{\pm0.1}_{4.1\sigma}$	$1.7^{\pm0.1}_{3.3\sigma}$	$†3.4^{\pm0.2}_{3.1\sigma}$	$‡1.7^{\pm0.3}_{3.3\sigma}$
OJ 014	$4.2^{\pm0.5}_{3.2\sigma}$	$4.1^{\pm0.4}_{2.6\sigma}$	$4.1^{\pm0.1}_{2.6\sigma}$	$‡4.4^{\pm0.9}_{3.6\sigma}$
PKS 0454−234	$3.6^{\pm0.2}_{3.2\sigma}$	$3.5^{\pm0.4}_{2.8\sigma}$	$3.5^{\pm0.4}_{2.4\sigma}$	$‡3.9^{\pm0.8}_{2.8\sigma}$
S5 0716+714⋆	$2.7^{\pm0.4}_{3.5\sigma}$	$2.6^{\pm0.4}_{2.8\sigma}$	$2.9^{\pm0.3}_{2.4\sigma}$	$‡2.9^{\pm0.8}_{2.8\sigma}$
	$0.9^{\pm0.1}_{3.0\sigma}$			$0.9^{\pm0.1}_{1.3\sigma}$
GB6 J0043+3426	$1.9^{\pm0.2}_{3.3\sigma}$	$1.9^{\pm0.4}_{2.6\sigma}$	$†3.9^{\pm0.2}_{2.3\sigma}$	$2.1^{\pm0.6}_{2.7\sigma}$
TXS 0518+211	$3.0^{\pm0.4}_{3.0\sigma}$	$3.1^{\pm0.4}_{2.4\sigma}$	$3.1^{\pm0.2}_{2.4\sigma}$	$‡3.2^{\pm0.5}_{2.7\sigma}$
87GB 164812.2+524	$2.8^{\pm0.9}_{2.2\sigma}$	$3.4^{\pm0.4}_{1.8\sigma}$	$3.0^{\pm0.1}_{2.2\sigma}$	$‡3.8^{\pm0.8}_{2.6\sigma}$
PKS 0447−439	$1.9^{\pm0.2}_{2.6\sigma}$	$1.8^{\pm0.2}_{2.0\sigma}$	$†4.0^{\pm0.4}_{2.0\sigma}$	$2.1^{\pm0.5}_{2.2\sigma}$
PKS 0426−380	$3.5^{\pm0.6}_{2.6\sigma}$	$3.6^{\pm0.5}_{2.0\sigma}$	$3.4^{\pm0.5}_{1.7\sigma}$	$‡3.4^{\pm0.6}_{2.1\sigma}$
PKS 0301−243	$2.1^{\pm0.2}_{2.7\sigma}$	$2.1^{\pm0.2}_{1.9\sigma}$	$†4.0^{\pm0.1}_{1.3\sigma}$	$2.2^{\pm0.2}_{2.1\sigma}$
S4 1144+40	$3.3^{\pm0.2}_{2.7\sigma}$	$3.3^{\pm0.5}_{1.5\sigma}$	$3.2^{\pm0.5}_{2.0\sigma}$	$‡3.4^{\pm0.9}_{1.7\sigma}$
PG 1246+586	$2.1^{\pm0.2}_{2.5\sigma}$	$2.2^{\pm0.1}_{1.5\sigma}$	$†4.2^{\pm0.1}_{1.1\sigma}$	$‡2.2^{\pm0.3}_{1.9\sigma}$
PKS 0250−225	$1.2^{\pm0.2}_{3.0\sigma}$	$1.2^{\pm0.1}_{1.6\sigma}$	$†2.4^{\pm0.1}_{1.4\sigma}$	$1.3^{\pm0.2}_{1.7\sigma}$
PKS 2255−282⋆	$1.4^{\pm0.1}_{2.2\sigma}$	$2.8^{\pm0.4}_{1.8\sigma}$	$2.7^{\pm0.2}_{1.7\sigma}$	$‡3.7^{\pm0.8}_{1.7\sigma}$
	$2.8^{\pm0.3}_{1.8\sigma}$	$1.4^{\pm0.1}_{1.0\sigma}$		$1.4^{\pm0.3}_{1.1\sigma}$
TXS 1902+556	$3.3^{\pm0.4}_{2.5\sigma}$	$3.3^{\pm0.3}_{1.4\sigma}$	$3.3^{\pm0.3}_{1.3\sigma}$	$‡3.4^{\pm0.7}_{1.6\sigma}$
S3 0458−02	$3.7^{\pm0.9}_{1.8\sigma}$	$4.1^{\pm0.6}_{1.2\sigma}$	$3.8^{\pm0.3}_{1.3\sigma}$	$4.4^{\pm0.7}_{1.5\sigma}$
MG2 J130304+2434	$2.0^{\pm0.2}_{2.0\sigma}$	$4.1^{\pm0.1}_{1.0\sigma}$	$†4.0^{\pm0.1}_{1.2\sigma}$	$4.1^{\pm0.6}_{1.1\sigma}$
PKS 2052−47⋆	$1.6^{\pm0.2}_{2.5\sigma}$	$3.1^{\pm0.3}_{1.1\sigma}$	$2.8^{\pm0.4}_{1.0\sigma}$	$3.3^{\pm0.3}_{1.2\sigma}$
		$1.4^{\pm0.2}_{2.0\sigma}$		
S4 0814+42	$2.2^{\pm0.2}_{2.0\sigma}$	$2.2^{\pm0.2}_{0.8\sigma}$	$2.2^{\pm0.3}_{0.8\sigma}$	$‡2.3^{\pm0.3}_{0.8\sigma}$
MG1 J021114+1051	$2.8^{\pm0.3}_{2.0\sigma}$	$1.7^{\pm0.1}_{0.8\sigma}$	$2.8^{\pm0.2}_{0.8\sigma}$	$‡4.6^{\pm0.7}_{0.9\sigma}$
TXS 0059+581	$4.0^{\pm0.6}_{1.7\sigma}$	$4.1^{\pm0.6}_{0.7\sigma}$	$4.2^{\pm0.1}_{0.8\sigma}$	$‡4.6^{\pm0.7}_{0.7\sigma}$
TXS 1452+516	$2.0^{\pm0.4}_{1.4\sigma}$	$2.0^{\pm0.2}_{0.7\sigma}$	$†4.3^{\pm0.4}_{0.5\sigma}$	$2.1^{\pm0.6}_{0.7\sigma}$
PKS 0208−512	$3.8^{\pm0.5}_{1.1\sigma}$	$3.7^{\pm0.4}_{0.1\sigma}$	$3.8^{\pm0.5}_{0.1\sigma}$	$‡4.6^{\pm0.9}_{0.2\sigma}$

Table A2. List of power-spectrum indices inferred by $ML-MCMC$ method for the PL and BPL of the PSD, considering the Poisson noise expressed by equation (4). The parameter 'A' is the normalization (rms^2/yr^{-1}) and $\nu_{Bending}$ the bending frequency. The Poisson noise is represented by 'C' (rms^2/yr^{-1}). The AIC values for both PSD models, as well as the RML for model comparison, are provided.

Association Name	C	A/PL Index	AIC	A/BPL Index/$\nu_{Bending}$	AIC	RML
PG 1553+113	$2.97\text{x}10^{-3}$	$1.91\text{x}10^{-2}\pm9.15\text{x}10^{-3}$ 1.25±0.13	−1453.90	$1.93\text{x}10^{-2}\pm7.84\text{x}10^{-3}$ 1.83±0.49 1.98±0.08	−1519.19	$6.62\text{x}10^{-15}$
PKS 2155−304	$1.62\text{x}10^{-3}$	$1.87\text{x}10^{-2}\pm8.59\text{x}10^{-3}$ 0.88±0.11	−1328.91	$4.75\text{x}10^{-2}\pm1.03\text{x}10^{-2}$ 0.88±0.09 1.19±0.22	−1488.91	$1.83\text{x}10^{-35}$
OJ 014	$3.42\text{x}10^{-3}$	$2.02\text{x}10^{-2}\pm8.26\text{x}10^{-3}$ 1.07±0.09	−1397.74	$1.10\text{x}10^{-1}\pm1.63\text{x}10^{-2}$ 2.67±0.27 0.81±0.29	−1690.12	$3.23\text{x}10^{-64}$
PKS 0454−234	$7.37\text{x}10^{-4}$	$2.11\text{x}10^{-2}\pm6.52\text{x}10^{-3}$ 1.16±0.07	−1701.75	$1.25\text{x}10^{-1}\pm0.13\text{x}10^{-2}$ 1.82±0.09 0.71±0.06	−1790.97	$4.22\text{x}10^{-20}$
S5 0716+714	$5.97\text{x}10^{-4}$	$1.91\text{x}10^{-2}\pm7.50\text{x}10^{-3}$ 0.78±0.08	−1905.83	$5.74\text{x}10^{-2}\pm5.60\text{x}10^{-3}$ 1.38±0.16 1.26±0.18	−2009.53	$3.02\text{x}10^{-23}$
GB6 J0043+3426	$1.83\text{x}10^{-2}$	$1.82\text{x}10^{-2}\pm6.61\text{x}10^{-3}$ 1.01±0.11	−2282.27	$3.55\text{x}10^{-2}\pm9.92\text{x}10^{-3}$ 1.86±0.26 1.97±0.39	−2384.97	$5.01\text{x}10^{-23}$
TXS 0518+211	$2.35\text{x}10^{-3}$	$2.13\text{x}10^{-2}\pm1.25\text{x}10^{-3}$ 1.37±0.11	−2221.78	$1.14\text{x}10^{-1}\pm2.93\text{x}10^{-2}$ 2.76±0.18 0.82±0.09	−2253.26	$1.45\text{x}10^{-7}$
87GB 164812.2+524	$1.53\text{x}10^{-2}$	$2.63\text{x}10^{-2}\pm7.77\text{x}10^{-3}$ 0.42±0.07	−1993.41	$4.62\text{x}10^{-2}\pm7.89\text{x}10^{-3}$ 5.34±0.41 0.53±0.02	−2042.38	$2.32\text{x}10^{-11}$
PKS 0447−439	$1.25\text{x}10^{-3}$	$2.78\text{x}10^{-2}\pm8.15\text{x}10^{-3}$ 0.62±0.09	−2349.50	$4.55\text{x}10^{-2}\pm7.14\text{x}10^{-3}$ 2.21±0.21 1.62±0.18	−2520.38	$7.83\text{x}10^{-38}$
PKS 0426−380	$8.33\text{x}10^{-4}$	$2.21\text{x}10^{-2}\pm7.06\text{x}10^{-3}$ 1.28±0.12	−1787.17	$6.10\text{x}10^{-1}\pm1.56\text{x}10^{-2}$ 1.51±0.13 0.11±0.07	−1921.43	$7.03\text{x}10^{-30}$
PKS 0301−243	$3.97\text{x}10^{-3}$	$1.73\text{x}10^{-2}\pm6.78\text{x}10^{-3}$ 1.08±0.20	−2411.60	$3.12\text{x}10^{-2}\pm8.13\text{x}10^{-3}$ 2.72±0.34 1.47±0.15	−2567.70	$1.26\text{x}10^{-34}$
S4 1144+40	$3.33\text{x}10^{-3}$	$2.07\text{x}10^{-2}\pm6.48\text{x}10^{-3}$ 1.58±0.13	−1516.63	$1.13\text{x}10^{-1}\pm2.38\text{x}10^{-2}$ 3.41±0.28 0.53±0.05	−1839.98	$6.11\text{x}10^{-71}$
PG 1246+586	$5.39\text{x}10^{-3}$	$1.75\text{x}10^{-2}\pm6.13\text{x}10^{-3}$ 1.09±0.05	−1986.96	$1.25\text{x}10^{-1}\pm1.58\text{x}10^{-2}$ 1.76±0.13 0.39±0.02	−1998.73	$2.78\text{x}10^{-3}$
PKS 2255−282	$5.44\text{x}10^{-3}$	$2.34\text{x}10^{-2}\pm7.14\text{x}10^{-3}$ 0.97±0.08	−1868.80	$1.56\text{x}10^{-1}\pm1.53\text{x}10^{-2}$ 2.13±0.22 0.39±0.04	−1895.91	$1.29\text{x}10^{-6}$
PKS 0250−225	$2.57\text{x}10^{-3}$	$2.63\text{x}10^{-2}\pm6.13\text{x}10^{-3}$ 0.88±0.087	−2363.85	$3.20\text{x}10^{-2}\pm1.21\text{x}10^{-3}$ 4.24±0.37 1.74±0.26	−2601.55	$2.43\text{x}10^{-52}$
TXS 1902+556	$4.46\text{x}10^{-3}$	$1.69\text{x}10^{-2}\pm7.18\text{x}10^{-3}$ 0.86±0.07	−2130.05	$1.25\text{x}10^{-1}\pm2.73\text{x}10^{-2}$ 1.47±0.08 0.31±0.01	−2252.84	$2.16\text{x}10^{-27}$
S3 0458−02	$3.51\text{x}10^{-3}$	$2.35\text{x}10^{-2}\pm1.28\text{x}10^{-3}$ 0.91±0.09	−2221.87	$1.56\text{x}10^{-1}\pm5.74\text{x}10^{-2}$ 1.17±0.10 0.21±0.09	−2253.30	$1.49\text{x}10^{-7}$
MG2 J130304+2434	$1.10\text{x}10^{-2}$	$1.82\text{x}10^{-2}\pm5.21\text{x}10^{-3}$ 0.86±0.13	−2302.85	$5.67\text{x}10^{-2}\pm1.45\text{x}10^{-3}$ 2.64±0.15 0.74±0.02	−2388.63	$2.36\text{x}10^{-19}$
PKS 2052−47	$2.08\text{x}10^{-3}$	$1.63\text{x}10^{-2}\pm6.56\text{x}10^{-3}$ 0.93±0.05	−2282.80	$1.75\text{x}10^{-1}\pm9.33\text{x}10^{-2}$ 1.19±0.12 0.14±0.07	−2296.20	$1.23\text{x}10^{-3}$
S4 0814+42	$3.14\text{x}10^{-3}$	$2.44\text{x}10^{-2}\pm2.11\text{x}10^{-3}$ 0.71±0.05	−2157.11	$5.58\text{x}10^{-2}\pm2.11\text{x}10^{-3}$ 3.17±0.37 0.81±0.05	−2217.64	$7.17\text{x}10^{-14}$
MG1 J021114+1051	$5.78\text{x}10^{-4}$	$2.21\text{x}10^{-2}\pm5.55\text{x}10^{-3}$ 0.58±0.06	−2245.71	$5.68\text{x}10^{-2}\pm1.28\text{x}10^{-3}$ 2.36±0.25 0.76±0.07	−2336.78	$1.67\text{x}10^{-20}$
TXS 0059+581	$8.48\text{x}10^{-3}$	$1.82\text{x}10^{-2}\pm1.28\text{x}10^{-3}$ 0.96±0.07	−2056.70	$6.53\text{x}10^{-2}\pm6.90\text{x}10^{-3}$ 3.84±0.28 0.77±0.09	−2110.71	$1.87\text{x}10^{-12}$
TXS 1452+516	$9.15\text{x}10^{-3}$	$1.83\text{x}10^{-2}\pm1.23\text{x}10^{-3}$ 0.86±0.05	−2102.64	$8.06\text{x}10^{-2}\pm5.38\text{x}10^{-3}$ 2.75±0.21 0.51±0.02	−2132.03	$4.16\text{x}10^{-7}$
PKS 0208−512	$6.14\text{x}10^{-4}$	$2.83\text{x}10^{-2}\pm1.45\text{x}10^{-3}$ 0.61±0.06	−2431.58	$6.03\text{x}10^{-2}\pm1.34\text{x}10^{-3}$ 2.66±0.17 0.86±0.05	−2617.92	$3.44\text{x}10^{-41}$

Table A3. Results of the influence on the test statistics of the power-law approach. Three different models are studied for a power law, considering the slopes and uncertainties provided in Table A2: [β_{min}, A_{min}], [β, A], [β_{max}, A_{max}].

Association Name	Model	LSP	GLSP	PDM	CWT
PG 1553+113	β_{min}=1.12 A_{min}=9.98x10^{-3}	4.4σ	4.0σ	3.5σ	3.2σ
	β=1.25 A=1.91x10^{-2}	3.7σ	3.5σ	3.2σ	2.7σ
	β_{max}=1.39 A_{max}=2.28x10^{-2}	3.1σ	3.0σ	2.8σ	2.5σ
PKS 2155−304	β_{min}=0.76 A_{min}=1.01x10^{-2}	2.8σ	2.8σ	2.1σ	2.0σ
	β=0.88 A=1.87x10^{-2}	2.5σ	2.5σ	1.7σ	1.7σ
	β_{max}=0.99 A_{max}=2.73x10^{-2}	2.3σ	2.2σ	1.2σ	1.5σ

Table A4. Results of the influence on the test statistics of the bending power-law approach. Three different models are studied for the bending power law, according to the slope, the bending frequency, and the normalization, according to the associated uncertainties: [α_{min}, $\nu_{Bending\_min}$, A_{min}], [α, $\nu_{Bending}$, A], [α_{max}, $\nu_{Bending\_max}$, A_{max}]. The symbol # indicates that the test statistic is constrained by the limited number of artificial LCs generated for the analysis.

Association Name	Model	LSP	GLSP	PDM	CWT
PG 1553+113	α_{min}=1.34 $\nu_{Bending\_min}$=1.89 A_{min}=1.15x10^{-2}	#4.9σ	#4.9σ	#4.5σ	4.6σ
	α=1.83 $\nu_{Bending}$=1.98 A=1.93x10^{-2}	#4.9σ	4.6σ	4.2σ	4.4σ
	α_{max}=2.32 $\nu_{Bending\_max}$=2.07 A_{max}=2.72x10^{-2}	4.8σ	4.6σ	4.0σ	3.9σ
PKS 2155−304	α_{min}=0.79 $\nu_{Bending\_min}$=0.96 A_{min}=4.65x10^{-2}	2.9σ	3.4σ	2.9σ	3.5σ
	α=0.88 $\nu_{Bending}$=1.19 A=4.75x10^{-2}	2.9σ	3.3σ	3.1σ	3.3σ
	α_{max}=0.98 $\nu_{Bending\_max}$=1.41 A_{max}=4.85x10^{-2}	2.8σ	3.1σ	3.0σ	3.3σ

Table A5. List of periods provided by the Markov Chain Monte Carlo sine fits and the Bayesian quasi-periodic oscillation methods following a similar structure as Table 1. The #in ARFIMA/ARIMA column indicates that the model used is ARIMA due to the LC being non-stationary (resulting from augmented Dickey-Fuller test, see Section 3.3). The period obtained with the ACF from the residuals generated from the original LC and the ARIMA/ARFIMA model is also listed. Note that there are some sources with two periods (organized by the test statistics), which are denoted by ⋆. Finally, Xs in the Dickey-Fuller and Box-Ljung columns indicate that the null hypothesis is rejected in such tests (Section 3.3). All periods are in years.

Association name	MCMC Sine fitting	ARFIMA/ARIMA Residuals	ACF	Dickey–fuller	Box-ljung
PG 1553+113⋆	2.1 ± 0.1	[17, 0.449, 18]	2.8 (2.0σ) 2.0 (1.5σ)	✓	✓
PKS 2155−304⋆	1.7 ± 0.1	[10, 0.435, 10]	1.6 (2.1σ) 1.0 (1.6σ)	✓	✓
OJ 014	4.4 ± 0.1	[19, 0.471, 15]	3.8 (1.6σ)	✓	✓
PKS 0454−234⋆	3.5 ± 0.1	[20, 0.493, 20]	2.0 (2.0σ) 1.2 (1.6σ)	✓	✓
S5 0716+714	2.7 ± 0.1	[12, 0.447, 14]	1.2 (1.6σ)	✓	✓
GB6 J0043+3426	1.8 ± 0.1	[9, 0.472, 10]	2.0 (2.1σ)	✓	✓
TXS 0518+211	$3.1^{+0.1}_{-0.8}$	[15, 0.333, 13]	2.9 (1.9σ)	✓	✓
87GB 164812.2+524023	$2.9^{+0.8}_{-0.1}$	[18, 0.445, 20]	2.0 (1.2σ)	✓	✓
PKS 0447−439⋆	$1.8^{+0.1}_{-0.6}$	[15, 0.45, 14]	1.5 (2.2σ) 2.5 (1.5σ)	✓	✓
PKS 0426−380⋆	3.2 ± 0.1	[14, 0.47, 14]	3.4 (2.3σ) 2.2 (1.9σ)	✓	✓
PKS 0301−243	$1.4^{+0.8}_{-0.1}$	[17, 0.451, 20]	1 (1.7σ)	✓	✓
S4 1144+40	3.5 ± 0.1	[18, 0.433, 19]	2.5 (2.0σ)	✓	✓
PG 1246+586	2.2 ± 0.1	[16, 0.436, 20]	3.5 (2.8σ)	✓	✓
PKS 0250−225	1.2 ± 0.1	#[5, 1, 8]	1.3 (1.5σ)	×	✓
PKS 2255−282	3.1 ± 0.1	[18, 0.441, 19]	2.8 (1.6σ)	✓	✓
TXS 1902+556	3.3 ± 0.1	[20, 0.41, 15]	3.4 (1.6σ)	✓	✓
S3 0458−02⋆	1.5 ± 0.2	[10, 0.453, 8]	3.8 (2.2σ) 2.1 (2.0σ)	✓	×
MG2 J130304+2434	1.2 ± 0.1	[19, 0.471, 20]	2.0 (2.1σ)	✓	✓
PKS 2052−47	2.6 ± 0.1	[18, 0.441, 19]	1.6 (1.9σ)	✓	✓
S4 0814+42	2.1 ± 0.1	[14, 0.451, 14]	3.1 (2.2σ)	✓	✓
MG1 J021114+1051	1.7 ± 0.1	[15, 0.414, 14]	2.6 (1.95σ)	✓	✓
TXS 0059+581	4.1 ± 0.1	[16, 0.391, 18]	3.9 (1.4σ)	✓	✓
TXS 1452+516	2.1 ± 0.1	[19, 0.448, 18]	1.7 (1.9σ)	✓	✓
PKS 0208−512	$4.0^{+0.5}_{-1.0}$	#[2, 1, 8]	1.2 (1.0σ)	×	×

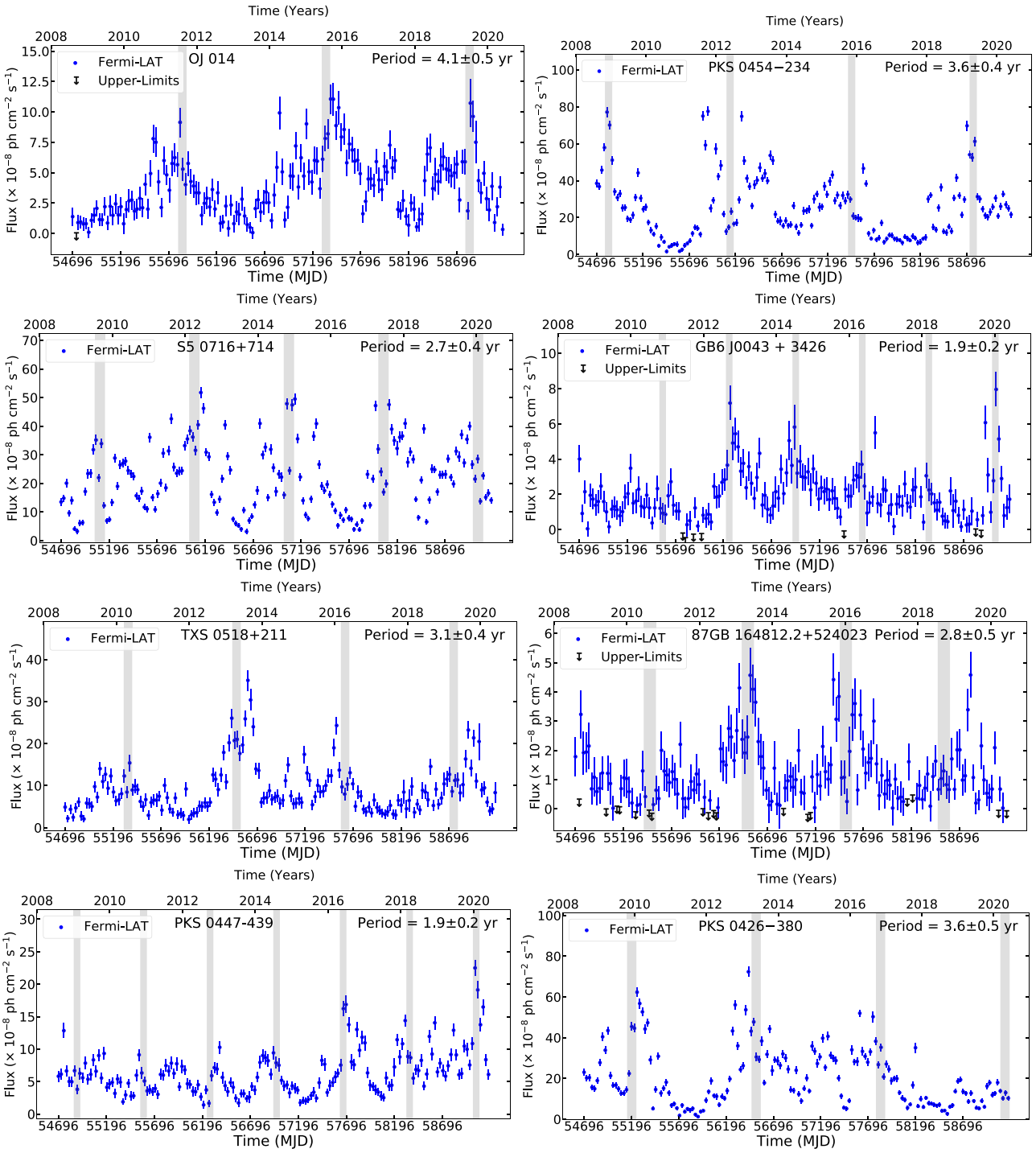

Figure A1. Light curves of the low-significance blazars presented in Table 1. The grey vertical bars approximate high-flux periods suggested by the period inferred by the methodology for the given blazar. The width of the grey bars indicates the uncertainty in the periodic signal.

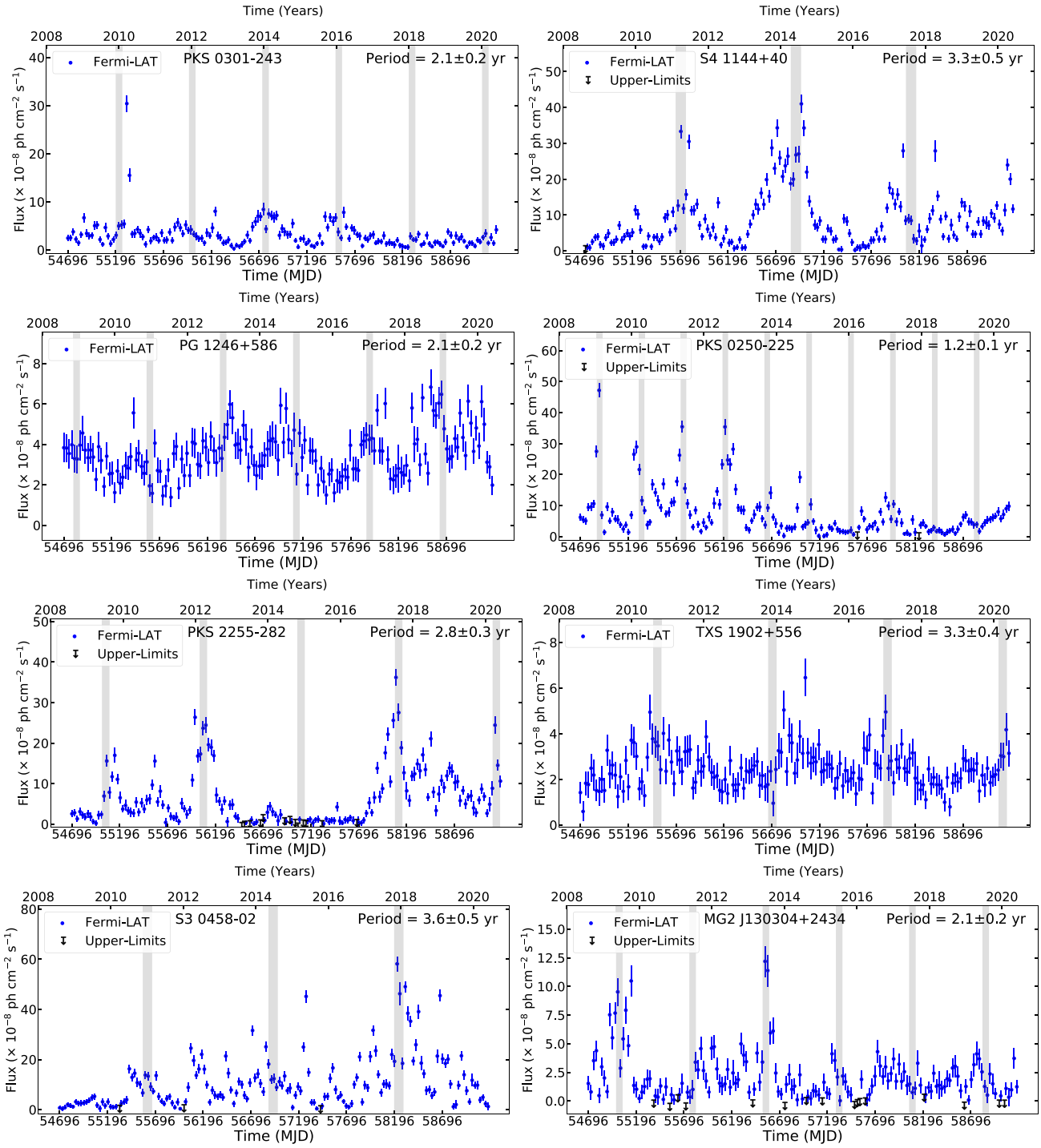

Figure A1. *Continued.*

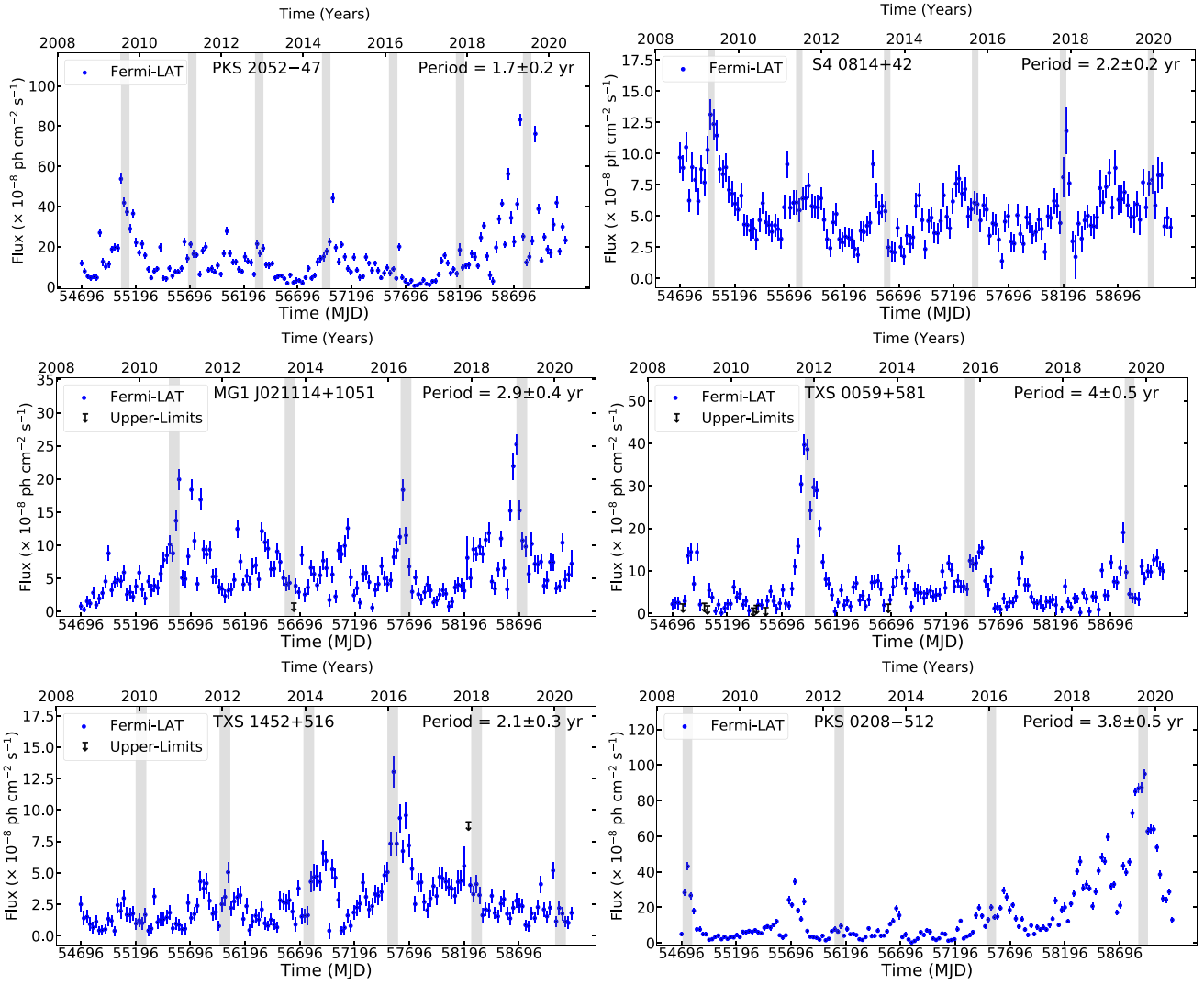

Figure A1. *Continued.*

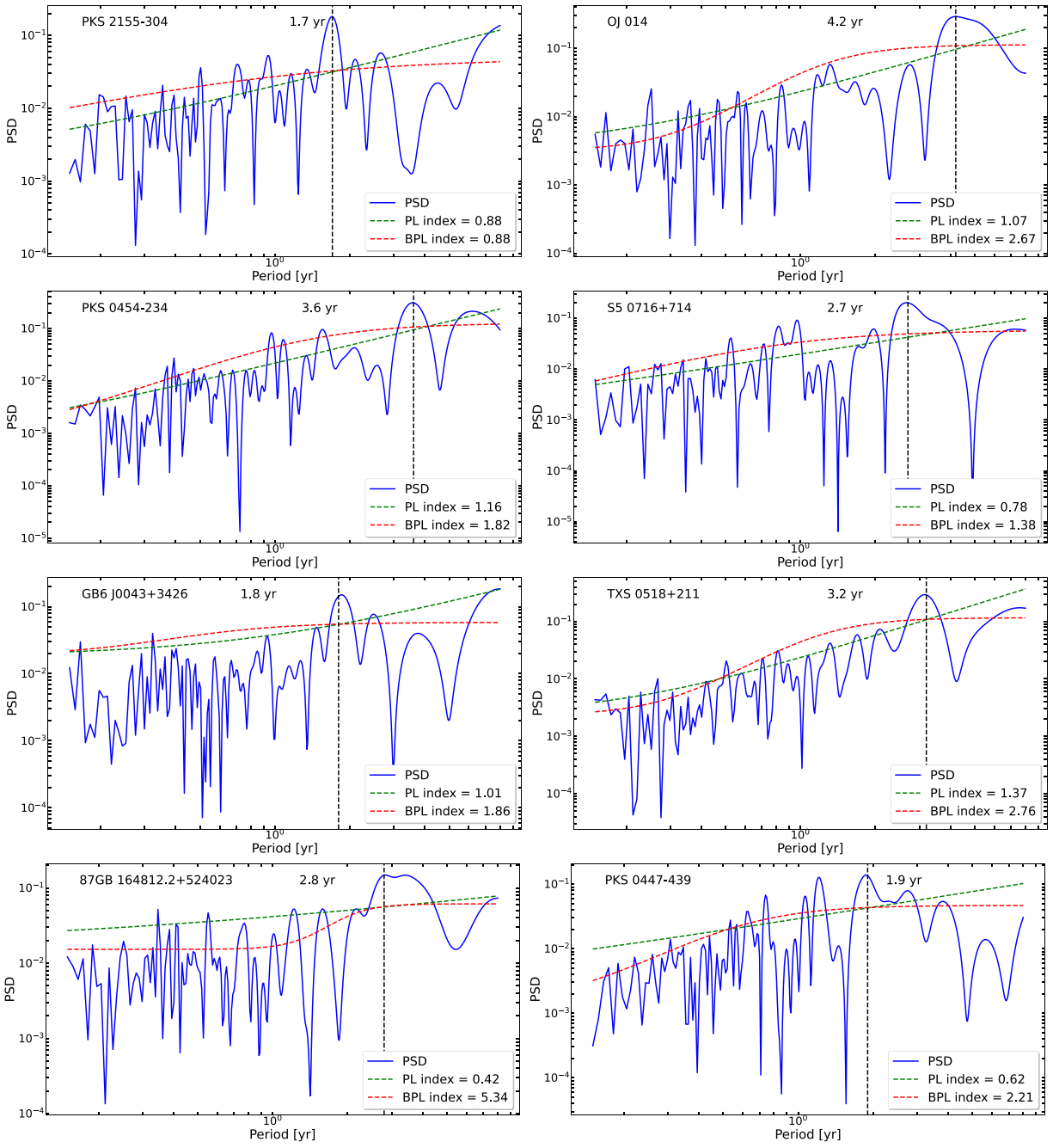

Figure A2. Power spectral densities according to the fit presented in Table A2.

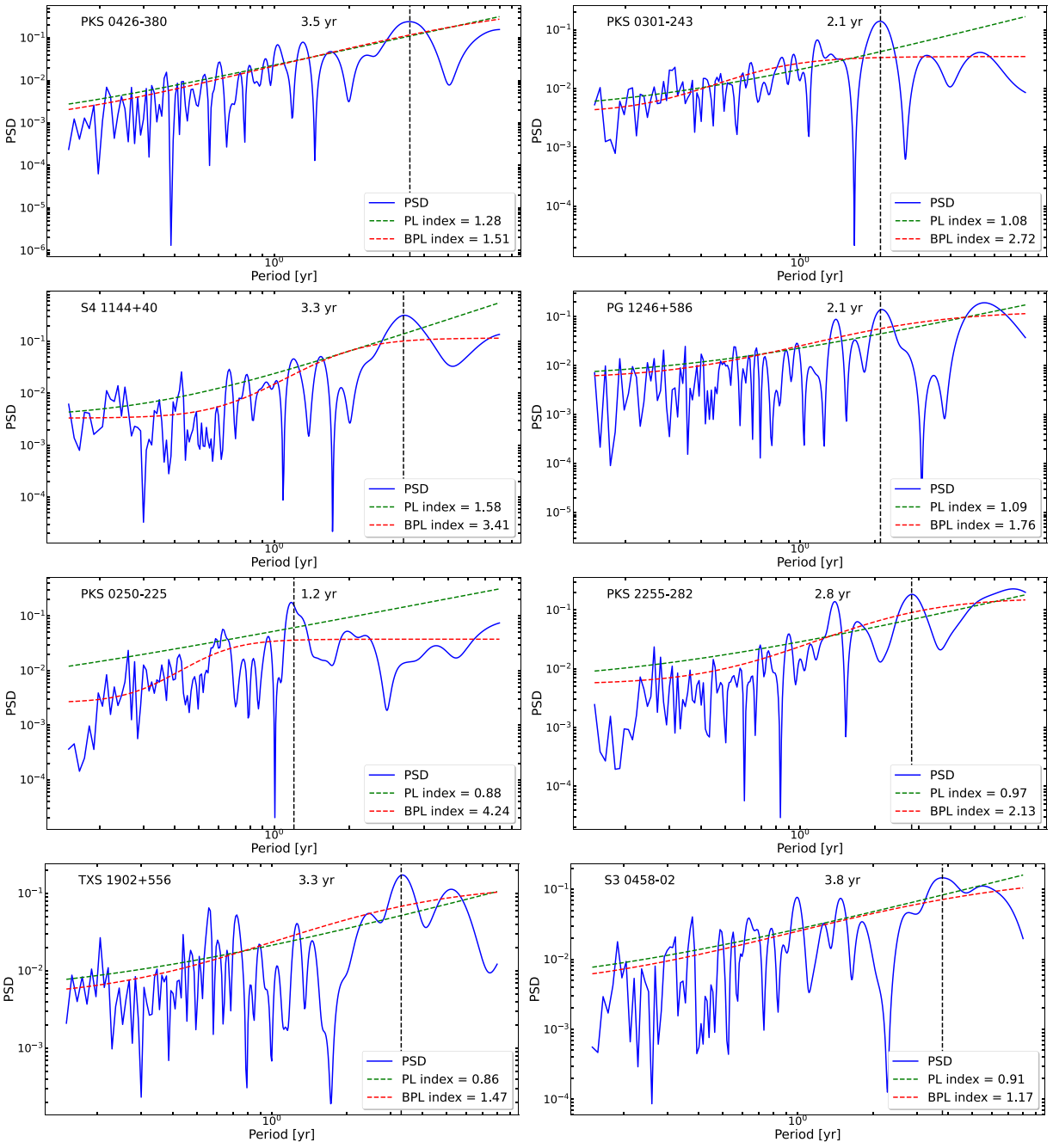

Figure A2. *Continued.*

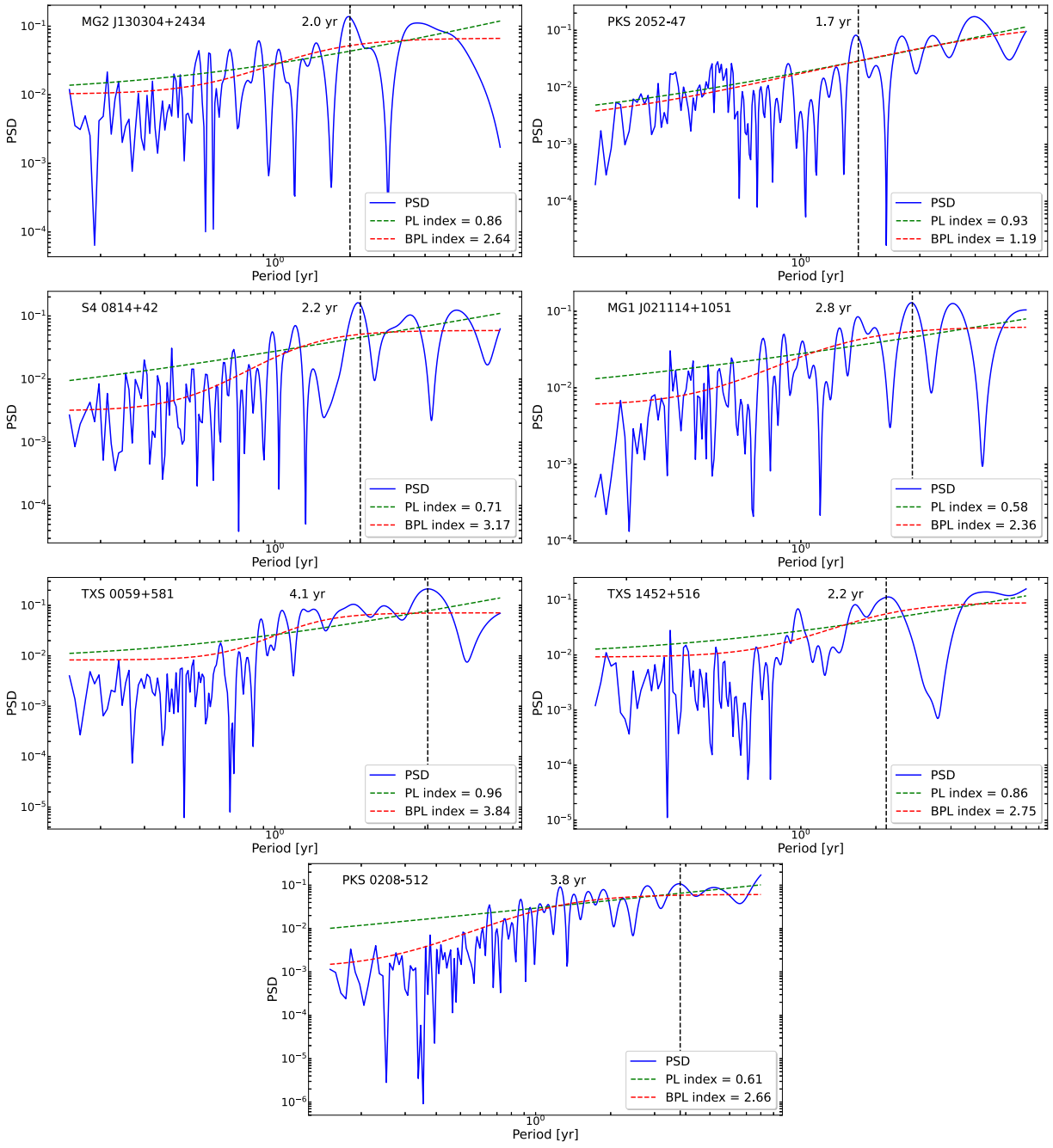

Figure A2. *Continued.*

This paper has been typeset from a TEX/LATEX file prepared by the author.